CD103$^+$CD56$^+$ ILCs Are Associated with an Altered CD8$^+$ T-cell Profile within the Tumor Microenvironment

Douglas C. Chung[1,2], Noor Shakfa[3], Jehan Vakharia[2], Kathrin Warner[2], Nicolas Jacquelot[2], Azin Sayad[2], SeongJun Han[1,2], Maryam Ghaedi[2], Carlos R. Garcia-Batres[2], Jules Sotty[2], Arvin Azarmina[2], Ferris Nowlan[3,4], Edward L.Y. Chen[3], Michael Zon[9,10,11,12], Alisha R. Elford[2], Ben X. Wang[2], Linh T. Nguyen[2], Miralem Mrkonjic[6,7], Blaise A. Clarke[6,8], Marcus Q. Bernardini[6,8], Benjamin Haibe-Kains[9,10,11,12], Sarah E. Ferguson[8,13], Sarah Q. Crome[1,14], Hartland W. Jackson[3,4,5], and Pamela S. Ohashi[1,2]

ABSTRACT

Immunotherapies have had unprecedented success in the treatment of multiple cancer types, albeit with variable response rates. Unraveling the complex network of immune cells within the tumor microenvironment (TME) may provide additional insights to enhance antitumor immunity and improve clinical response. Many studies have shown that NK cells or innate lymphoid cells (ILC) have regulatory capacity. Here, we identified CD103 as a marker that was found on CD56$^+$ cells that were associated with a poor proliferative capacity of tumor-infiltrating lymphocytes in culture. We further demonstrated that CD103$^+$CD56$^+$ ILCs isolated directly from tumors represented a distinct ILC population that expressed unique surface markers (such as CD49a and CD101), transcription factor networks, and transcriptomic profiles compared with CD103$^-$CD56$^+$ NK cells. Using single-cell multiomic and spatial approaches, we found that these CD103$^+$CD56$^+$ ILCs were associated with CD8$^+$ T cells with reduced expression of granzyme B. Thus, this study identifies a population of CD103$^+$CD56$^+$ ILCs with potentially inhibitory functions that are associated with a TME that includes CD8$^+$ T cells with poor antitumor activity. Further studies focusing on these cells may provide additional insights into the biology of an inhibitory TME.

Introduction

Immune regulation is composed of a complex multilayered network of cellular and molecular pathways that regulate the immune system to prevent tissue damage and autoimmunity. Innate lymphoid cells (ILC) are a heterogeneous population of cells that primarily reside in peripheral tissues and are capable of rapidly orchestrating innate and adaptive immunity in response to pathogenic and physiologic signals (1). The ILC family includes NK cells, ILC1s, ILC2s, ILC3s, and lymphoid tissue inducer cells (1). ILC1s are defined by the expression of CD127, a lack of surface markers that define other immune subsets, and the absence of CRTH2 or cKit expression (2, 3). However, distinguishing ILC1s from NK cells has been challenging as various lineage-defining markers can vary depending on the tissue microenvironment and activation status (4). Moreover, ILC1s have been shown to express surface markers similar to NK cells (e.g., C-X-C chemokine receptor type 6; ref. 5). ILC2s secrete type 2 cytokines including IL-4, IL-5, IL-9, IL-13, and amphiregulin, express the transcription factor (TF) GATA3, and play a role in clearing parasite infections (1). ILC3s secrete IL-17, IL-22, and GM-CSF and contribute to intestinal homeostasis and response to bacterial infections (1).

Human NK cells in the periphery have been historically subdivided based on the level of expression of CD56 and CD16 (6). CD56^{dim}CD16$^{+/-}$ cells were initially described as potent cytolytic effector cells that express high levels of IFN-γ and cytolytic molecules (including perforins and granzymes), whereas CD56^{bright}CD16$^-$

[1]Department of Immunology, University of Toronto, Toronto, Canada. [2]Tumour Immunotherapy Program, Princess Margaret Cancer Centre, University Health Network, Toronto, Canada. [3]Systems Biology Program, Lunenfeld-Tanenbaum Research Institute, Mount Sinai Health System, Toronto, Canada. [4]Department of Molecular Genetics, University of Toronto, Toronto, Canada. [5]Ontario Institute of Cancer Research, Toronto, Canada. [6]Department of Laboratory Medicine and Pathobiology, University of Toronto, Toronto, Canada. [7]Department of Pathology and Laboratory Medicine, Mount Sinai Hospital, Toronto, Canada. [8]Division of Gynecologic Oncology, University Health Network, Toronto, Canada. [9]Princess Margaret Cancer Centre, University Health Network, Toronto, Canada. [10]Medical Biophysics, University of Toronto, Toronto, Canada. [11]Structural Genomics Consortium, Toronto, Canada. [12]Vector Institute for Artificial Intelligence, Toronto, Canada. [13]Department of Obstetrics and Gynecology, University of Toronto, Toronto, Canada. [14]Toronto General Hospital Research Institute, Ajmera Transplant Centre, University Health Network, Toronto, Canada.

Current address for D.C. Chung: Genentech, South San Francisco, California; current address for N. Jacquelot: Department of Biochemistry and Molecular Genetics, Cumming School of Medicine, University of Calgary, Calgary, Canada; Department of Microbiology, Immunology and Infectious Diseases, Cumming School of Medicine, University of Calgary, Calgary, Canada; Arnie Charbonneau Cancer Research Institute, Calgary, Canada; current address for S. Han: Department of Immunology, Blavatnik Institute, Harvard Medical School, Boston, Massachusetts; Department of Cell Biology, Blavatnik Institute, Harvard Medical School, Boston, Massachusetts; Evergrande Center for Immunologic Diseases, Harvard Medical School and Brigham and Women's Hospital, Boston, Massachusetts; and current address for M. Zon: School of Biomedical Engineering, McMaster University, Ontario, Canada; Michael DeGroote School of Medicine, McMaster University, Ontario, Canada.

Corresponding Author: Pamela S. Ohashi, Princess Margaret Cancer Centre, University Health Network, 610 University Avenue, Toronto M5G 2C4, Ontario, Canada. E-mail: pam.ohashi@uhn.ca

Cancer Immunol Res 2025;13:527–46

doi: 10.1158/2326-6066.CIR-24-0151

cells have reduced lytic abilities and increased expression of cytokines. However, recent studies have found that CD56 brightness does not necessarily correlate with NK cell function (7, 8), challenging the current nomenclature of NK cells. For example, NK cells treated with either IL-15 (7, 9) or IL-12 in the presence of the OVCAR carcinoma cell line (10), or IL-2 and membrane-bound IL-21 on feeder cells (8), led to the induction of $CD56^{bright}$ NK cells with enhanced degranulation and cytotoxicity *in vitro*. Moreover, IL-21–induced $CD56^{bright}$ NK cells had an increased ability to clear autologous tumors in a patient-derived xenograft murine model. $CD56^{bright}CD16^{+}$ NK cells derived from melanoma metastasis in the lymph node that were activated with IL-15 had enhanced cytotoxic function (11). Although several studies have characterized $CD56^{bright}$ cells in human cancers (12, 13), the functional role of these cells within the tumor microenvironment (TME) is unclear.

Beyond the conventional roles of ILCs, there is growing evidence that they also have potent immunosuppressive roles with similar mechanisms that mirror regulatory T cells (Tregs; ref. 14), adding to the complexity of immune regulatory networks. Notably, NK-like regulatory cells have been shown to directly suppress T cells in colitis (15), autoimmunity (16–22), GVHD (refs. 23–25), and chronic viral infections (14, 26–30). In addition, ILC2s and ILC3s have also demonstrated diverse mechanisms of suppression in a variety of contexts (14, 30).

ILCs with inhibitory properties have been recently identified in the context of cancer (14, 31–34). For example, $NKp46^{-}$ ILC3s from a mouse model of hepatocellular carcinoma suppressed the proliferation of $CD8^{+}$ T cells and increased apoptosis *in vitro* (33). Moreover, human NK cells that have been previously cocultured with primary sarcoma tumor cells were able to subsequently suppress $CD4^{+}$ T-cell proliferation and IFN-γ production (34). In our previous work, we identified $CD56^{+}$ immunoregulatory ILCs from *in vitro*–expanded tumor-infiltrating lymphocyte (TIL) cultures derived from patients with epithelial ovarian carcinoma (EOC; ref. 32). $CD56^{+}$ ILCs could suppress autologous $CD4^{+}$ T-cell and $CD8^{+}$ T-cell expansion *in vitro*, in part through an NKp46-dependent mechanism. Because these immunoregulatory $CD56^{+}$ ILCs were found in slow growing TIL cultures (supplemented with high-dose IL-2), our next goal was to examine whether we could identify their counterparts in primary EOC tumors. In this study, we found that CD103 is a marker for a distinct population of $CD56^{+}$ ILCs and explored their properties and the corresponding TME from primary EOC tumors.

Materials and Methods

Study design

This research study was conducted in accordance with the guidelines of the Declaration of Helsinki and was approved by the University Health Network (UHN) Institutional Research Ethics Board (10-0335). Informed consent was obtained from all study participants. Surgical specimens and fluids were obtained through UHN Biospecimen Services. The tonsil, spleen, and appendix were retrieved from the Mount Sinai Services Surgical Pathology Department under Research Ethics Board 20-0178-E. Peripheral blood mononuclear cells were retrieved from consented healthy donors through Miltenyi Biotec (150-000-450).

Sample preparation

Tumor specimens were retrieved from the UHN Biospecimen Program through surgical resection of 54 patients diagnosed with EOC. Patient characteristics are summarized in Supplementary Table S1. Fresh tumor specimens were enzymatically digested [1 mg/mL collagenase I (catalog no. C5138, Sigma-Aldrich), 10 μg/mL pulmozyme (DIN: 02046733, Hoffmann-La Roche), 2 mmol/L L-glutamine (catalog no. 25030-081, Gibco), and 100 μg/mL amphotericin B (catalog no. 15290-018, Gibco) in RPMI-1640 (catalog no. 11875093, Thermo Fisher Scientific)] using a Gentle MACs Dissociator (Miltenyi Biotec). Tumor digests were cryopreserved in human serum (catalog no. 106-512, GeminiBio) containing 10% DMSO (catalog no. 472301, Sigma-Aldrich) in liquid nitrogen tanks and were thawed prior to analysis.

Flow cytometry and cell sorting

Cells were washed twice in FACS buffer [PBS, 2% FBS (catalog no. A15-701, PAA Laboratories), and 0.05% sodium azide (catalog no. 7144.8-16, RICCA)] or PBS, followed by staining with fixable viability dye eFluor 780 (catalog no. 65-0865-14, 1:1,000, eBioscience) or eFluor 506 (catalog no. 65-0866-14, 1:800, eBioscience) and FcR blocking (catalog no. 564220, 1:200, BD Biosciences, RRID: AB_2869554) in PBS at 4°C for 20 minutes. The cells were washed and subsequently stained for surface marker antibody cocktails at 4°C for 30 minutes (see Supplementary Table S2 for the list of antibodies used). The cells were washed and fixed with eBioscience Foxp3 Fixation/Permeabilization buffer (catalog no. 00-5523-00, Thermo Fisher Scientific) for 30 minutes and washed with 1× permeabilization buffer. The cells were stained for 60 minutes at 4°C with an intracellular antibody cocktail in 1× permeabilization buffer (see Supplementary Table S2 for the list of antibodies used). Data were acquired on a BD LSRFortessa (BD Biosciences) at the Princess Margaret Flow Cytometry Core Facility using FACSDiva v.9.0.1 (BD Biosciences) and analyzed using FlowJo software v10.8.1 (FlowJo LLC, RRID: SCR008520). Cell sorting was performed on a Beckman MoFlo Astrios or BD FACSAria Fusion (BD Biosciences) by the Princess Margaret Flow Cytometry Core Facility. Intratumoral Tregs were gated as previously described (35). $CD56^{+}$ ILCs were negatively gated for lineage markers and were defined as either $CD3^{-}TCR\alpha\beta^{-}TCR\gamma\delta^{-}CD14^{-}CD19^{-}CD20^{-}CD34^{-}CD123^{-}CD303^{-}Fc\varepsilon RI\alpha^{-}$ or $CD3^{-}CD14^{-}CD19^{-}$.

Survival analysis from publicly available datasets

Gene signatures were developed from bulk RNA sequencing (RNA-seq) analysis of $CD56^{+}$ inhibitory ILCs derived from TIL cultures (32) using the top 25 most negative and positive genes determined by log fold change values. Genes that contributed positively to the signature score included *DNAH2*, *COL18A1*, *HSPA2*, *COL11A2*, *RAB26*, *FAM43A*, *IER5L*, *CTSL*, *TTN*, *JUNB*, *JUN*, *SIGLEC17P*, *COL9A2*, *KIAA1683*, *MST1*, *RHOB*, *HIST2H2BD*, *XKR6*, *KANK3*, *FOSB*, *ADAMTS17*, *MAFB*, *SNAI1*, *DUSP1*, and *MYO15B*. Genes that contributed negatively to the signature score included *PARP9*, *ARHGAP11A*, *WDR76*, *OAS1*, *MMS22L*, *ASPM*, *TENM1*, *MX1*, *ATAD5*, *A2M*, *KIR2DL3*, *KIR3DL1*, *KIR3DX1*, *BRIP1*, *CHMP4C*, *KIAA1324L*, *ZNF280B*, *IFI44L*, *KIR2DL1*, *CDKN3*, *NOSTRIN*, *NUTM2F*, *DNAH11*, *CHRNA7*, and *ISY1-RAB43*. The genes contributing positively and negatively were assigned a weight of +1 and −1, respectively. The full list of genes and their weights is provided in Supplementary Table S1.

Bulk RNA-seq datasets of tumors from patients with high-grade serous ovarian carcinoma (HGSC) were curated from GSE9891, GSE17260, GSE26193, GSE30161, GSE49997, and TCGAOVARIAN (36–41). These datasets were chosen because they included at least 50% of the genes in our signature. Patients within these datasets that

were in the top 50th percentile in expression of CD56 were included. Patients were scored based on the expression of the CD56$^+$ inhibitory ILC gene signature and were split into two groups (i.e., high vs. low using the mean of signature scores to determine the 50th percentile threshold) for downstream survival analysis using recurrence-free survival data (RFS). Data were censored at 10 years. A random effects model was used to account for variability across different dataset, and D index was used as the statistical measure to assess the prognostic ability of our gene signatures.

Bulk RNA-seq and analysis

RNA was extracted from sorted CD103$^+$CD56$^+$Lin$^-$ ILCs (a total of 250,900 cells) and CD103$^-$CD56$^+$Lin$^-$ ILCs (a total of 282,800 cells) matched from four patient samples using RNeasy Mini Kit (catalog no. 74104, Qiagen) according to the manufacturer's instructions. After quantity and quality assessments using Agilent Bioanalyzer RNA 6000 Nano Kit (catalog no. 5067-1511, Agilent) and KAPA SYBR FAST qPCR kit (catalog no. KK44602, Roche), RNA libraries were prepared, and rRNA were removed using SMARTer Stranded Total RNA-seq Kit V3 – Pico Input Mammalian (catalog no. 634485, Takara Bio). Libraries were normalized, pooled, and loaded onto Illumina NovaSeq V1.5 cartridges for cluster generation, and sequencing was performed on a NovaSeq 6000 instrument (Illumina). Using the paired-end 101 bp protocol, approximately 40 million reads per sample were produced. RNA-seq was performed by the Princess Margaret Genomics Center.

RNA-seq FASTQ files were mapped using STAR aligner v2.5.2b (RRID: SCR_004463; ref. 42) with human transcript coordinates from Human Release 29 GENCODE (GRCh37; RRID: SCR_014966; ref. 43). Reads were summarized per gene using RSEM v1.3.0 (RRID: SCR_00262; ref. 44). Bioconducter (RRID: SCR006442; ref. 45) BioMart (RRID: SCR_019214; ref. 46) was used to map the Ensemble transcript IDs to NCBI gene IDs and UniGene symbols. Immunoglobulin genes were removed before further analysis. Differential gene expression analysis was performed using DESeq2 (RRID: SCR_015687; ref. 47), and *P* values were adjusted for multiple testing using Benjamini and Hochberg FDR correction (48).

GSEA v4.2.3 (RRID: SCR_003199; ref. 49) was used to perform gene set enrichment, with FDR-adjusted *P* values < 0.15 considered significantly enriched. The Hallmark, Canonical Pathways, Transcription Factor Targets, and Gene Ontology gene set collections from MSigDB v2022.1 (RRID: SCR_016863) were tested for enrichment. Next, Cytoscape v3.9.1 (RRID: SCR_003032; ref. 50) EnrichmentMap v.3.3.4 (RRID: SCR_016052; ref. 51) was used to find clusters of enriched gene sets with large numbers of shared genes. Thus, gene sets in each cluster were likely enriched because of the differential expression of shared member genes. Only clusters with five or more gene sets (nodes) were included in the figure, and cluster names were manually curated for clarity based on the names of gene sets in each cluster.

Single-cell RNA sequencing

Three separate single-cell RNA sequencing (scRNA-seq) experiments were performed and cells were stained, sorted, and pooled depending on the specific experiments listed below.

(i) CD45$^+$ cells were mixed with CD45$^-$ cells in a 1:1 ratio for each sample (OV348, OV744, and OV749);
(ii) CD45$^+$CD56$^+$CD127$^{+/-}$Lin$^-$ ILCs were mixed with CD45$^+$CD56$^-$CD127$^+$Lin$^-$ ILCs in a 1:1 ratio for each sample (OV699, OV702, and OV710)
(iii) CD45$^+$Lin$^+$ immune cells (OV699, OV702, and OV710).

Staining was performed as per the manufacturer's guidelines and in consultation with Princess Margaret Genomics Center. For dataset (i), cells were stained with FcR blocking antibody (catalog no. 564220, 1:200, BD Biosciences, RRID: AB_2869554) in PBS at 4°C for 20 minutes. The cells were then stained with fixable viability dye eFluor 780 (catalog no. 65-0865-14, 1:1000, eBioscience) and surface antibody cocktails before FACS. For datasets (ii) and (iii), cells were also hashtagged and pooled with four other tissue/tumor types and cellular indexing of transcriptomes and epitopes sequencing was performed. Briefly, cells were stained with FcR blocking antibody (catalog no. 564220, 1:200, BD Biosciences, RRID: AB_2869554) and DNA-barcoded tetramer specific to MR1 (catalog no. 405261, BioLegend) and CD1d (catalog no. 405271, BioLegend) to identify mucosal-associated invariant T cells and NK T cells, respectively, at 4°C for 40 minutes. Human MR1 5-OP-RU and CD1d PBS-57 tetramers and their control counterparts (i.e., MR1 6-FP and CD1d unloaded) were provided by NIH and incubated with biotinylated monomers with TotalSeq-C oligo-barcoded streptavidin (i.e., catalog no. 405261, 405271, 405273, and 405275, respectively, BioLegend) as per the manufacturer's instructions. Cells were stained with fluorescence surface antibody cocktail for FACS at 4°C for 30 minutes. Finally, the cells were stained with a cocktail of Hashtag DNA-barcoded antibodies targeting β2M and CD298 (catalog no. 394661, 394663, 394665, 394667, and 394669; RRIDs: AB_2801031, AB_2801032, AB_2801033, AB_2801034, and AB_2801035; BioLegend) and DNA-barcoded antibodies targeting unique surface antigens. For the latter, TotalSeq-C Human Universal Cocktail targeting 130 unique antigens (catalog no. 399905, RRID: AB_2876728, BioLegend), along with antibodies targeting cKit (catalog no. 313243, RRID: AB_2810474, BioLegend), CRTH2 (catalog no. 350131, RRID: AB_2814279, BioLegend), and CD307a (catalog no. 374413, RRID: AB_2876703, BioLegend), was used. Live cells were then sorted and pooled before sequencing. For (ii) and (iii), lineage markers were defined as CD3$^-$TCRαβ$^-$TCRγδ$^-$CD14$^-$CD19$^-$CD20$^-$ CD34$^-$CD123$^-$CD303$^-$FcεRIα$^-$.

Samples were prepared at the Princess Margaret Genomics Center using Chromium Single Cell 5′ v2 Reagent Kit (catalog no. PN-1000263, 10× Genomics) according to the manufacturer's instructions. Library size was determined using Agilent High Sensitivity DNA Kit (5067-4626, Agilent). Samples were pooled and quantified using Qubit dsDNA HS Assay Kit (Q32851, Qubit) on the Qubit 2.0 Fluorometer. Pools were sequenced with an S2 flow cell on a NovaSeq 6000 platform (Illumina) to a targeted depth of 50,000 reads per cell. FASTQ files were aligned to GRCh38, and counts data were assembled using CellRanger v6.1.2 (10× Genomics, SCR_023221).

Quality control and preprocessing included the removal of cells with low features (≤200), high features (≥5,000), and/or a high fraction of mitochondrial genes. Moreover, genes expressed in less than 10 cells were excluded. For datasets (i), (ii), and (iii), 15,742 cells, 1,374 cells, and 23,289 cells passed the threshold, respectively, and were included in the analysis. After log-normalization of the data, samples were batch corrected using Seurat's integration function (52), which used reciprocal principal component analysis (PCA; ref. 53). After scaling the data and PCA, cells were clustered using Seurat's built-in clustering function (resolutions for datasets i, ii, and iii were 1.0, 0.5, and 0.5, respectively). Uniform Manifold Approximation and Projection (UMAP) for

dimension reduction was then used to obtain pairs of values (UMAP1 and UMAP2) summarizing the expression profile of each cell for visualization purposes. These coordinates were plotted with colors determined by the Seurat cluster assignment of each cell. Cell clusters were annotated following examination of differentially expressed markers obtained by Seurat FindAllMarkers in the initial round of clustering, and its cell sub-clustered to identify subpopulations. For dataset (i), $CD56^+$ILCs underwent unsupervised clustering (resolution = 0.2) and resulted in subclusters $CD103^+CD56^+$ ILCs (90 cells) and $CD103^-CD56^+$ ILCs (344 cells). For dataset (ii), $CD103^+CD56^+$ ILCs underwent unsupervised clustering (resolution = 0.5) and resulted in two subclusters: sc0 (256 cells) and sc1 (106 cells). Plots were generated using ggplot2 v3.3.6. $CD56^+CD3^-$ cells were gated by protein expression using CITEViz (54).

Single-cell regulatory network inference and clustering analysis

Single-cell regulatory network inference and clustering (SCENIC) analysis was performed on $CD56^+$ ILC clusters from scRNA-seq (dataset i) to reconstruct gene regulatory networks by identifying regulons (or TFs and their target genes; ref. 55). pySCENIC (v.0.12.0, Python 3.10.6, RRID: SCR_025802) identifies potential gene targets for each TF based on co-expression (GENIE3/GRNBoost2), selects potential direct binding targets based on DNA motif analysis (RcisTarget), and analyzes network activity in each individual cell. Only regulons that reached *P* adjusted value of <0.01 were included in output figures.

TIL cultures

Methods for TIL expansion are described by Nguyen and colleagues (56). Single-cell suspensions of TILs were plated at 1×10^6 cells/well in a Nunc Cell-Culture Treated 24 well plate (catalog no. 142475, Thermo Fisher Scientific) at 37°C and 5% CO_2. The cells were cultured in 2 mL of complete media comprising Iscove's modified Dulbecco's medium (catalog no. 12440-046, Gibco), 10% human serum (catalog no. 106-512, GeminiBio), 25 mmol/L HEPES (catalog no. 15630-080, Gibco), 100 μg/mL penicillin/streptomycin (catalog no. 17-602E, Lonza), 2 mmol/L L-glutamine (catalog no. 25030-081, Gibco), 10 μg/mL gentamicin (catalog no. 15290-018, Gibco), 0.05 mmol/L 2-Mercaptoethanol (catalog no. 21985-023, Gibco), and 6,000 IU/mL human recombinant IL-2 (i.e., Proleukin, Novartis) for 4 weeks. Media were replenished three times a week. TILs were split when confluent and were combined, mixed, and replated. "Rapidly expanding TILs" refer to TIL cultures that yielded $\geq 4 \times 10^6$ cells by 4 weeks, and "Slow or not expanding TILs" refer to TIL cultures that yielded $<4 \times 10^6$ cells by 4 weeks. The cells were processed for flow cytometry analysis.

Coculture of $CD103^+CD56^+Lin^-$ ILCs and T cells directly from tumors

Intratumoral $CD103^+CD56^+Lin^-$ ($CD3^-CD14^-CD19^-$) ILCs and $CD45^+$ immune cells (excluding $CD56^+Lin^-$ ILCs) were sorted using FACS from viably frozen samples of primary HGSC tumors ($n = 4$). $CD45^+$ immune cells were stained with 10 μmol/L cell proliferation dye eFluor 450 (catalog no. 65-0842-90, eBioscience) in PBS for 15 minutes at 4°C. $CD103^+CD56^+Lin^-$ ILCs were cocultured with $CD45^+$ immune cells (5×10^4 cells/well) in a 1:3 or 1:5 (suppressor:responder) ratio with soluble anti-CD3 (1 μg/mL, catalog no. 555337, BD Biosciences) for 4 days. All cell cultures were completed in RPMI-1640 complete media (catalog no. 11875119, Invitrogen) containing 10% FCS (catalog no. A15-701, PAA Laboratories), 2 mmol/L L-glutamine (catalog no. 25030-81, Gibco), 100 μg/mL penicillin–streptomycin (catalog no. 15140-122, Gibco), and 0.05 mmol/L 2-Mercaptoethanol (catalog no. M7522, Sigma-Aldrich). In a separate assay, $CD103^+CD49a^+CD56^+Lin^-$ ILCs were cocultured with 10,000 or 15,000 autologous $CD8^+$ T cells (1:1 or 1:13 suppressor to responder ratio) with soluble anti-CD3 (2 μg/mL, catalog no. 555337, BD Biosciences) and anti-CD28 (2 μg/mL, catalog no. 555726, BD Biosciences) for 3 to 4 days. CD49a was used in these assays to increase purification of these cells, although majority of $CD103^+CD56^+Lin^-$ ILCs were $CD49a^+$. To increase survival of intratumoral T cells, IL-2 (100 IU) or $CD25^-CD4^+$ autologous T cells (1:1 ratio of $CD8^+$ T cells and $CD25^-CD4^+$ T cells) were added into the cultures. The cells were incubated in Nunc MicroWell 96-well polystyrene microplates (catalog no. 12-565-66, Thermo Fisher Scientific) at 37°C and 5% CO_2. Precision Count Beads (catalog no. 424902, BioLegend; 10,000 beads/well) were added to retrieve absolute cell numbers from wells. The cells were analyzed on flow cytometry to identify changes in the cytolytic marker granzyme B (GZMB; AF700, QA16A02, 1:50, BioLegend), the activation marker CD25 (PE, M-A251, 1:50, BioLegend), and the proliferation marker Ki-67 (FITC, 20Raj1, 1:25, BioLegend).

Imaging mass cytometry

Preparation and sample staining

A cohort of eight HGSC samples (Supplementary Table S1) was included in this analysis. No statistical method was used to predetermine sample size, and all samples were stained simultaneously. Tissue samples were sectioned at 4 μmol/L thickness and formalin-fixed, paraffin-embedded at University Health Network with the Immune Profiling Team in Toronto. Tissue sections were baked at 60°C for 1 hour and deparaffinized in xylene for 30 minutes, followed by rehydration in a graded series of alcohol (ethanol:deionized water) at 100:0, 96:4, 90:10, 80:20, and 70:30 for 5 minutes each. Slides were placed in 1× TBS for 10 minutes following the last step in the series. In a decloaking chamber at 95°C, heat-induced epitope retrieval was performed in Tris-EDTA buffer (pH 9.2) for 30 minutes After complete cooling, the slides were incubated in blocking buffer [3% BSA and 5% horse serum (H0146, Sigma-Adlrich) in 1× TBS] at room temperature for 1 hour. Tissue on the slides was circled with a hydrophobic pen and samples were incubated in blocking buffer containing primary antibodies at appropriate concentrations at 4°C in a wet chamber. Tissue samples were washed in 1× TBS three times for 5 minutes each followed by a 5-minute incubation step in iridium at a dilution of 1:1,000 to counterstain slides. The slides were then washed in 1× TBS three times for 5 minutes again, briefly rinsed in ddH_2O to remove any salt, and dried before imaging mass cytometry (IMC) measurements. The antibody panel described in Supplementary Table S2 was used to stain the tissue sections.

Antibody optimization and conjugation

Antibodies were optimized on different control tissues including tonsil, spleen, appendix, and HGSC (see Supplementary Table S2 for a list of antibodies used). Initial immunofluorescence staining was performed to ensure antibody specificity and co-localization. Slide preparation followed the same steps as outlined in the previous section, and all samples were stained simultaneously. The slides were incubated in blocking buffer containing primary antibodies at 4°C in a wet chamber overnight followed by washing in 1× TBS three times for 5 minutes each. Tissues were then incubated in blocking buffer containing fluorescent secondary antibody [with either Goat anti-Rabbit IgG Alexa Fluor 488 (catalog no. A27034,

Invitrogen), Goat anti-Mouse IgG Alexa Fluor 488 (catalog no. A11029, Invitrogen), Goat anti-Mouse IgG Alexa Fluor 555 (catalog no. A21424, Invitrogen), or Goat anti-Rabbit IgG Alexa Fluor 555 (catalog no. A27039, Invitrogen)] at room temperature for 1 hour. The slides were then washed in 1× TBS three times for 5 minutes again and then counterstained with DAPI (2 μg/mL) for 5 minutes and washed again in 1× TBS three times for 5 minutes Coverslips were mounted using Prolong gold anti-fade (Thermo Fisher Scientific) and imaged. All antibody conjugations were performed at the Lunenfeld-Tanenbaum Research Institute according to the manufacturer's instructions (Maxpar X8 Multi-Metal Antibody Labeling Kit, Fluidigm). Metal-tagged antibodies were stored in a Candor Antibody Stabilizer (CANDOR Bioscience) at 4°C.

Image acquisition

Image acquisition and single-cell quantification and clustering were blinded to patient identifiers and clinical metadata. Acquisition order was performed randomly, independently of patient. IMC images were acquired at a resolution of roughly 1 μm. Cores were laser-ablated at a frequency of 200 Hz in a rastered pattern using the Hyperion Imaging System (Standard BioTools). Ablated tissue aerosol was ionized using inductively coupled plasma, and resulting isotopic ion reporters were quantified using time-of-flight mass spectrometry to infer protein abundance. Raw data were compiled using the Standard BioTools commerical acquisition software. All image acquisitions were successful and processed, whereby nearly each entire whole section was acquired in a number of regions of interest per patient sample.

Spillover correction

Due to the nature of IMC application, spillover of signal from one channel into another results in contamination between markers. As such, each individual metal-tagged antibody was mixed with trypan blue at 1:1 and spotted onto an agarose-coated slide and dried. Quantification by IMC of all metal isotopes was performed. A spillover matrix measuring the contamination between channels was generated and signal spillover between channels was corrected using functions from the CATALYST R package (RRID: SCR_017127; ref. 57).

Data processing, transformation, and normalization

Images were viewed to qualitatively assess spatial profiles in histoCAT (58). Data were converted into TIFFs and segmented into single cells using Mesmer (Deepcell, RRID: SCR_022197; ref. 59), which is available through our analysis pipeline at https://github.com/JacksonGroupLTRI/ImcPQ (58). Single-cell masks were generated using DNA, CD45, pan-cytokeratin, E-cadherin, and SMA to identify nuclear and membrane boundaries of cells. Single-cell expression data for 37 channels and DNA (Ir191 and Ir193) were outputted. The data were not transformed, and all analysis was performed on raw measurements. To remove "noise", the data were censored at the 99.9th percentile to remove outliers. *Z*-score of the mean across samples for each marker was applied to visualize using heatmaps. For UMAP generation (PhenoGraph clustering), data were normalized to the 99th percentile. Image analysis and segmentation were performed in Jupyter Notebook (RRID: SCR_018315) using Python.

Analysis and network generation

The single-cell IMC analysis pipeline was implemented in R. After segmentation with Deepcell into single-cell data, cell types were labeled using gating strategies. Each individual marker used for cell-type gating was visualized by histograms and by Cytomapper (60), and the cells selected by each cutoff were compared against original images to confirm gating accuracy. Combinatorial gates were employed to identify each population of interest (i.e., PanCK$^-$Ecadherin$^-$SMA$^-$Vimentin$^-$CD45$^+$CD3$^+$CD8$^+$). CD103$^+$CD56$^+$ILCs were gated as lineage negative cells (PanCK$^-$SMA$^-$Vim$^-$CD3$^-$CD20$^-$CD14$^-$CD15$^-$CD16$^-$CD123$^-$CD127$^-$CD117$^-$). A contact-based network representation of the segmentation mask was created with the Griottes package (61), an algorithm designed to generate a network representation and pairwise interactions. First-degree neighbors of each cell were extracted. Paired *t* tests were performed to find significant contact-based interactions between cell types. Dimensionality reduction of the dataset was initially carried out using PCA, followed by cell clustering with PhenoGraph (RRID: SCR_016919) and visualization using UMAP. Populations -1 and 38 were removed because of the small cell numbers which may represent debris. All statistical tests were conducted using R packages, and graphical representations were created using GraphPad (Prism 10, RRID: SCR_000306).

Statistical analysis

Statistical significance was determined by a two-tailed Student *t* test, one-way ANOVA, or two-way ANOVAs using appropriate multiple corrections depending on experimental conditions. For Kaplan–Meier curves, significance was determined by the log-rank (Mantel–Cox) test. The *n* values used to calculate statistics are defined and indicated in figure legends. Significance is indicated within figures or figure legends.

Data availability

Datasets generated during the current study are available online with Gene Expression Omnibus number GSE276966 and GSE276563. Code generated during data analysis will be available on Zenodo (RRID: SCR_004129) via the following link: https://zenodo.org/records/13743867. All other data generated in the study are available in the article and its supplementary files or from the corresponding author upon reasonable request.

Results

CD103 marks a population of CD56$^+$ cells potentially linked with poor outcome

To identify potential markers of inhibitory ILCs, we examined CD56$^+$Lin$^-$ cells from slow-growing TIL cultures, compared with those in rapidly expanding cultures, and found an increased proportion of cells expressing CD103 (**Fig. 1A** and **B**). We then further characterized CD103-expressing CD56$^+$ ILCs using multiparametric flow cytometry using cells directly isolated from surgically resected tumors from patients with EOC. First, we found that intratumoral Lin-negative CD56$^+$ ILCs expressed distinct surface markers and TFs compared with ILC1s, ILC2s, NKp46$^+$ ILC3s, and NKp46$^-$ ILC3s/ILC progenitors (Supplementary Fig. S1A and S1B). In addition, the CD103-expressing CD56$^+$ ILCs were preferentially found in primary ovarian tumors, and to some extent patient ascites, but were absent in peripheral blood from healthy donors (**Fig. 1C**; Supplementary Fig. S1C). This is consistent with previous studies that have identified CD103 as a transmembrane heterodimer involved in cell adhesion and tissue retention and as a common marker of tissue-resident lymphocytes (62, 63).

Although CD56 has been used to identify NK cells with canonical antitumor and antiviral cytotoxic functions (64), recent studies have demonstrated the extensive heterogeneity within the CD56$^+$ ILCs including subsets with noncanonical functions (i.e., angiogenic,

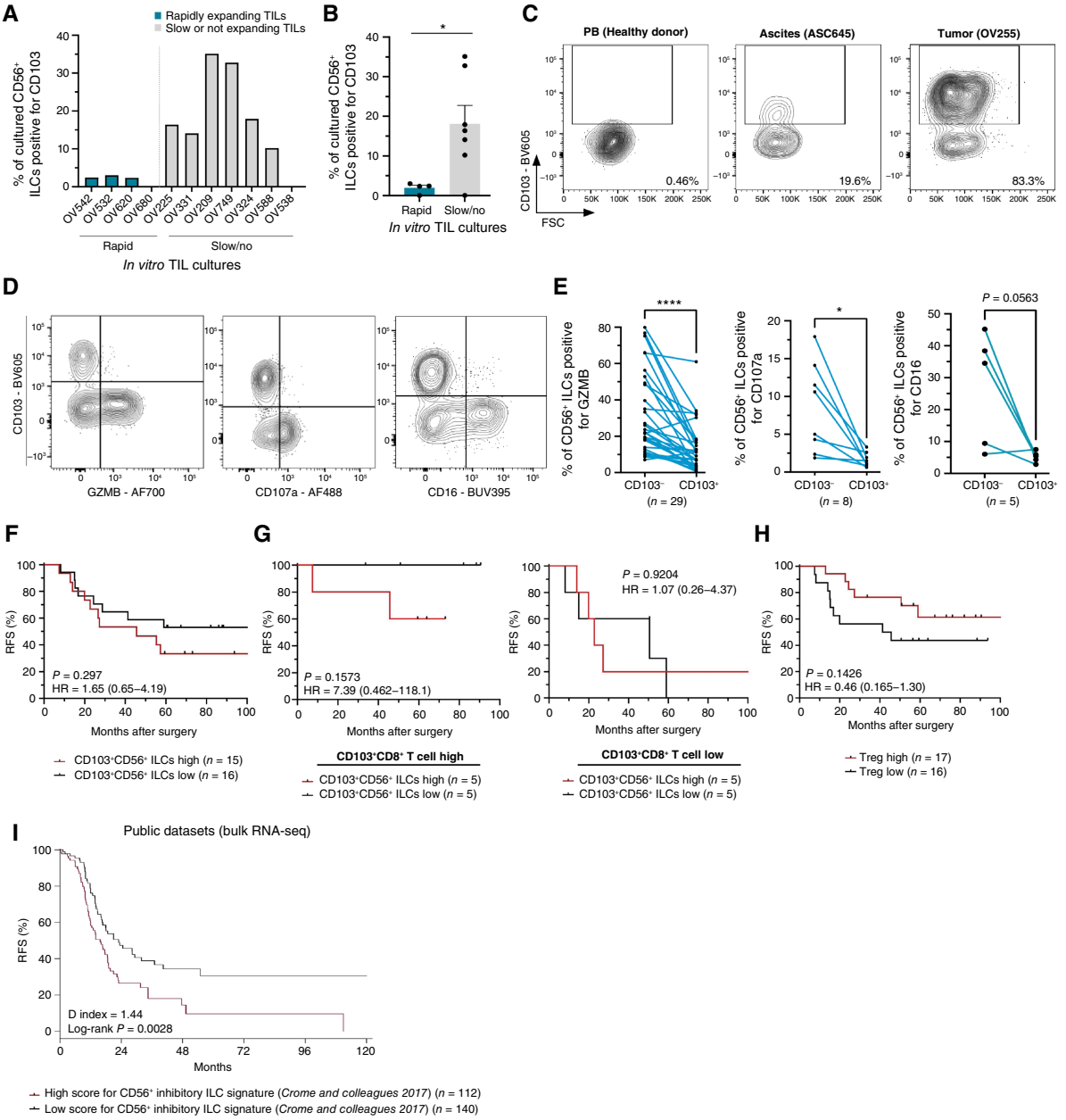

Figure 1.

CD103 may define a population of CD56$^+$Lin$^-$ cells with immunoregulatory function. **A** and **B,** TILs were cultured *in vitro* in high-dose IL-2 (6,000 IU/mL) for 4 weeks. The proportion of CD56$^+$ ILCs expressing CD103 is shown in TIL cultures that were slow- or non-expanding (<4 × 10^6 cells) compared with rapidly expanding TIL cultures (≥4 × 10^6 cells). A two-tailed Student *t* test was used, and variance is shown as SEM (**B**). **C,** Representative contour plots of CD103 in CD56$^+$Lin$^-$ (CD3$^-$TCRαβ$^-$TCRγδ$^-$CD14$^-$CD19$^-$CD20$^-$CD34$^-$CD123$^-$CD303$^-$FcεRIα$^-$) ILCs from healthy donor peripheral blood (PB) samples, ascites, and tumors. Expression of markers associated with cytolysis (i.e., GZMB, CD107a, and CD16) in CD103$^+$CD56$^+$Lin$^-$ ILCs and CD103$^-$CD56$^+$Lin$^-$ ILCs were analyzed by flow cytometry and representative samples shown as contour plots (**D**) and pairwise comparisons using a two-tailed Student *t* test (**E**). Kaplan–Meier curves showing differences in RFS between patients with EOC stratified based on characteristics within the TME (**F–H**). **F,** CD103$^+$CD56$^+$Lin$^-$ ILC High tumors had ≥60% of CD56$^+$ ILCs expressing CD103, and CD103$^+$CD56$^+$Lin$^-$ ILC Low had ≤40% of CD56$^+$Lin$^-$ ILCs expressing CD103. **G,** Patients were stratified into four groups based on CD103 expression on CD56$^+$Lin$^-$ ILCs and CD8$^+$ T cells, including (i) ILC high / CD8 high (left), (ii) ILC low / CD8 high (left), (iii) ILC high / CD8 low (right), and (iv) ILC low / CD8 low (right). ILC high–designated and low–designated tumors expressed CD103 in the top or bottom 50th percentile, respectively. CD8 T cell high and low were designated similarly. **H,** Patients were stratified based on whether they were in the top (Treg high) or bottom (Treg low) 50th percentile in their proportions of PD1^{int}ICOS^{hi}CD4$^+$ Tregs. *P* values and HRs were calculated using the log-rank and Mantel–Haenszel tests, respectively. **I,** CD56$^+$ immunoregulatory gene signature was developed from Crome and colleagues (Ref. 32; 2017) and applied to bulk RNA-seq datasets curated from GSE9891, GSE17260, GSE26193, GSE30161, GSE49997, and TCGAOVARIAN. Survival analysis of patients with ovarian carcinoma was conducted using RFS, and survival curve groups were determined by high ($n = 140$) or low ($n = 112$) expression of the CD56$^+$ immunoregulatory gene signature. A random effect model was used when combining estimators (D index). *, $P < 0.05$; ****, $P < 0.0001$. FSC, forward scatter.

cytokine-producing, and immune regulation; refs. 13, 65–68). Flow cytometry analysis of CD103$^+$CD56$^+$ ILCs showed that GZMB expression was not detectable, along with very low to undetectable expression of the degranulation marker CD107a and the antibody-dependent cellular cytotoxicity protein CD16 compared with CD103$^-$CD56$^+$ ILCs in the tumor (**Fig. 1D** and **E**). The CD103$^+$CD56$^+$ ILC population looked homogeneous in terms of the expression of these markers that were evaluated, supporting the idea that they represent a defined subset of cells. The reduction in cytotoxicity-related proteins in CD103$^+$CD56$^+$ ILCs suggests a noncytolytic role within the TME, although this does not exclude the possibility that cytotoxic functions may be upregulated upon further activation or polarization of this population.

To determine whether CD103$^+$CD56$^+$ ILCs are associated with clinical prognosis, we analyzed viably frozen samples from 32 patients for the proportion of CD103 expression on CD56$^+$ ILCs by flow cytometry. We found that tumors with a high abundance of CD103$^+$CD56$^+$ ILCs (≥60% of ILCs expressing CD103) had a trend, although not statistically different, toward reduced RFS compared with tumors with low abundance of CD103$^+$CD56$^+$ ILCs (≤40% of ILCs expressing CD103; **Fig. 1F**). Tissue-resident CD8$^+$ T cells have been shown to correlate with improved prognosis in the high-grade serous subtype of EOC (69) and play an important role in antitumor immunity (69, 70). To further refine this analysis, we examined the impact of the CD103$^+$CD56$^+$ cells in tumors with high numbers of tissue resident CD8$^+$ T cells. We found an association, although not statistically significant, between CD103$^+$CD56$^+$ ILCs and a trend toward reduced RFS to occur in patients with high proportion of CD103$^+$CD8$^+$ T cells (**Fig. 1G**). We also evaluated whether the presence of Tregs correlated with patient prognosis in our patient cohort and we found that they were associated with an opposite trend toward an increased RFS (**Fig. 1H**). To validate our findings with a larger cohort of patients with ovarian carcinomas, we developed a gene expression signature score based on bulk RNA-seq data of CD56$^+$ inhibitory ILCs derived from slow-growing TILs from Crome and colleagues (Supplementary Table S1; ref. 32). We then applied this signature score to a curated list of transcriptomic data of tumors from patients with ovarian carcinoma (36–41). Survival analysis showed a statistically significant difference, with patients having a high CD56$^+$ inhibitory ILCs signature ($n = 112$) being associated with a lower RFS compared with those with a low score for this signature ($n = 140$; **Fig. 1I**). Notably, the survival analysis from this larger cohort (**Fig. 1I**) showed similar kinetics with our flow cytometry cohort (**Fig. 1F**), with the split between the CD56$^+$-high and -low signature occurring at a similar time frame. Overall, these findings suggest that CD103$^+$CD56$^+$ ILCs may play an influential role within the TME and are associated with a trend toward poor clinical outcomes.

CD103$^+$CD56$^+$ ILCs exhibit a distinct transcriptomic profile compared with CD103$^-$CD56$^+$ ILCs

To further understand the biology of the CD103$^+$CD56$^+$ ILCs, we performed bulk RNA-seq on sorted, patient-matched populations of CD103$^+$CD56$^+$ ILCs and CD103$^-$CD56$^+$ ILCs ($N = 4$). CD103$^+$CD56$^+$ ILCs showed a distinct transcriptomic profile and grouped separately in a PCA from CD103$^-$CD56$^+$ ILCs (**Fig. 2A** and **B**; Supplementary Fig. S2A; Supplementary Table S3). Gene set enrichment analysis (ref. 49), followed by clustering of gene sets based on shared genes, revealed an enrichment of gene networks involved in cytokine signaling (i.e., IL-2, STAT5, IL-9, IL-37, and TPO), cell-cycle processes, and metabolic functions (i.e., glycogen synthesis and degradation and retinoic acid signaling) in CD103$^+$CD56$^+$ ILCs (**Fig. 2C** and **D**; Supplementary Fig. S2B; Supplementary Table S4). Correspondingly, CD103$^+$CD56$^+$ ILCs also had an enriched expression of genes encoding for IL-15 (i.e., *IL15RA*), IL-2 (i.e., *IL2RB* and *IL2RG*), and IL-27 (i.e., *IL27RA*) receptors (Supplementary Fig. S2C), suggesting a potential role for these cytokines in modulating the functions of these cells. Moreover, CD103$^+$CD56$^+$ ILCs were enriched in the gene expression of chemokine *CCL5* and the cytokine *IL-32*. Although CD103$^+$CD56$^+$ ILCs had a reduced expression of cytolytic molecules (**Fig. 1D** and **E**), there was an increased protein and gene expression of ENTPD1 (ATP ectonucleotidases) and TIGIT, both often associated with exhaustion or inhibitory mechanisms (**Fig. 3A** and **B**; Supplementary Fig. S2D) and the proliferation marker Ki67 (Supplementary Fig. S2D). In addition, there was an enrichment in co-stimulatory molecules *TMIGD2* (encoding for CD28H) and *KIR2DL4* (**Fig. 3A**). CD28H binds to B7 family member HHLA-2, inducing T-cell proliferation and cytokine production through AKT-dependent signaling cascade (71). KIR2DL4 is an activation receptor for nonclassical MHC class I molecule HLA-G (72). These findings suggest that CD103$^+$CD56$^+$ ILCs have been activated and may have distinct functions within the TME.

In contrast, CD103$^-$CD56$^+$ ILCs were more enriched in gene networks associated with canonical NK cell functions (i.e., allograft rejection, leukocyte migration, and leukocyte degranulation; **Fig. 2C** and **D**; Supplementary Fig. S2E; Supplementary Table S4). For example, CD103$^-$CD56$^+$ ILCs were enriched in expression of genes encoding Toll-like receptors (i.e., *TLR1 and TLR10*), activating receptors (i.e., *LILRA2* and *KLRF1*), and cytolysis-related molecules (i.e., *FCGR3A* and *GZMB*; **Fig. 3A**). Furthermore, CD103$^-$CD56$^+$ ILCs exhibited increased expression of class II HLA (i.e., *HLA-DMA*, *HLA-DMB*, *HLA-DOA*, *HLA-DQB1*, *HLA-DPB1*, *HLA-DRB1*, *HLA-DPA1*, *HLA-DRA*, and *HLA-DQA1*), suggesting a potential role in antigen presentation or an activated phenotype (Supplementary Fig. S2F; refs. 73–77). These findings suggest that CD103$^+$CD56$^+$ ILCs are transcriptomically distinct from CD103$^-$CD56$^+$ ILCs.

As expected, CD103$^+$CD56$^+$ ILCs expressed increased levels of genes associated with tissue-homing and retention (i.e., *CD69*, *CXCR6*, *ITGA7*, *ITGA1*, and *ITGAE*; ref. 62) but a decrease in genes associated with tissue egress (i.e., *CD62L*, *CCR7*, *ITGA5*, *ITGAX*, *KLF2*, *KLF4*, *S1PR1*, and *SELL*; Supplementary Fig. S2C). Zhou and colleagues (78) previously reported that CD49a-expressing tissue-resident group 1 ILCs suppressed antiviral T cells in the liver of LCMV-infected mice. Moreover, tissue-resident group 1 ILCs in the decidua are involved in tissue remodeling and protection against fetal loss during pregnancy (79). Consistent with a tissue retention–like phenotype, intratumoral CD103$^+$CD56$^+$ ILCs had reduced protein expression of the tissue-egress marker CD49e (encoded by *ITGA5*) and an increased expression of the tissue retention marker CD69 compared with CD103$^-$CD56$^+$ ILCs (**Fig. 3B** and **C**; Supplementary Fig. S2D). Moreover, CD103$^+$CD56$^+$ ILCs almost all uniformly expressed CD49a by flow cytometry (**Fig. 3B** and **C**), consistent with a tissue retention profile that has been previously described to have inhibitory roles.

CD103$^+$CD56$^+$ ILCs also had an increased expression of genes previously reported to be upregulated in inhibitory ILCs (i.e., *CD7* and *CD244*; refs. 32, 80). The increased expression of CD7 and other markers upregulated in inhibitory CD56$^+$ ILCs from TIL cultures (i.e., GITR, NKp30, and NKp46; ref. 32) were validated by flow cytometry (**Fig. 3B**; Supplementary Fig. S2D). We previously found that CD56$^+$ ILCs from TIL cultures inhibited T cells

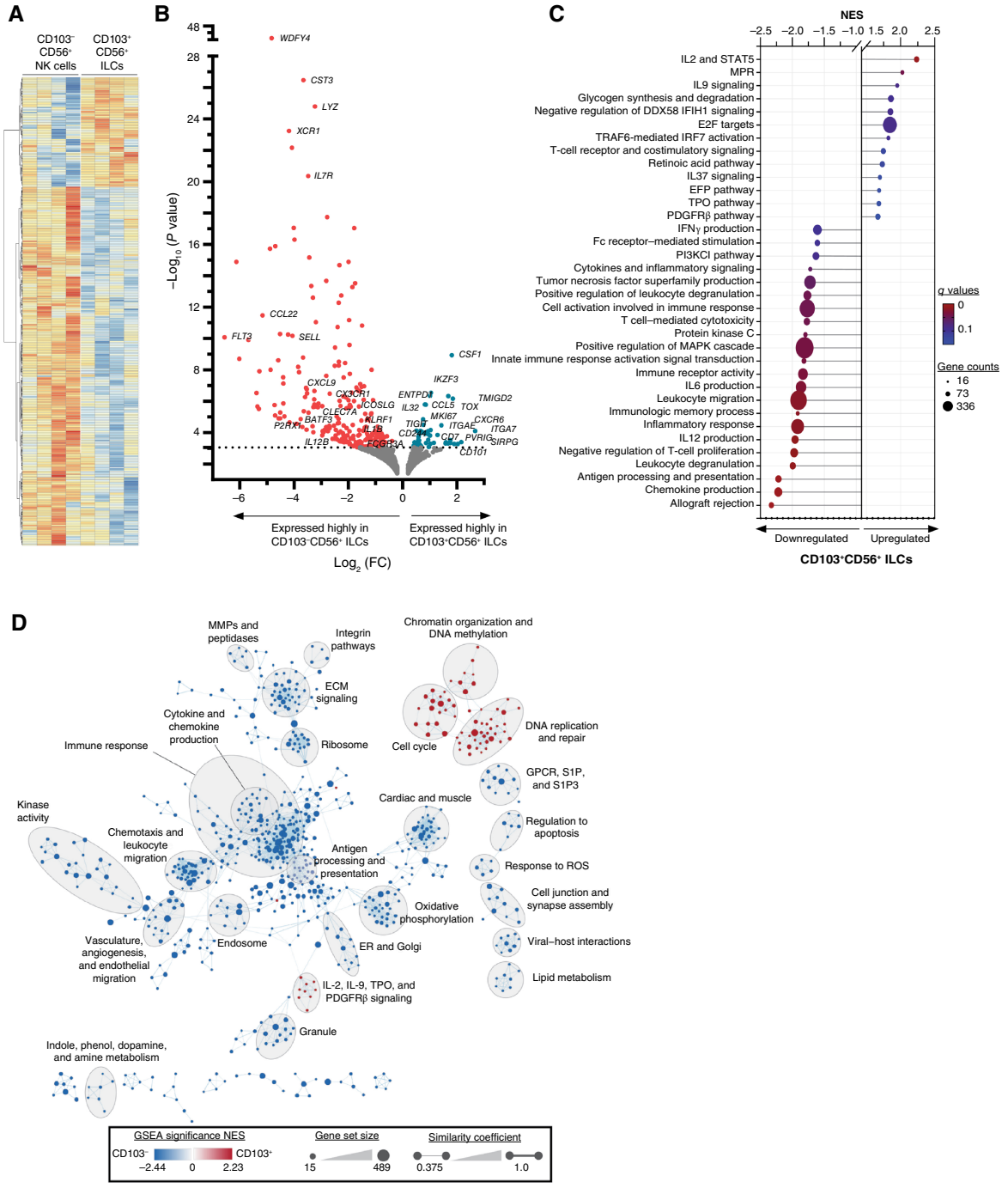

Figure 2.

CD103$^+$CD56$^+$Lin$^-$ ILCs exhibit a distinct transcriptomic profile from CD103$^-$CD56$^+$Lin$^-$ NK cells. RNA was extracted and sequenced from FACS-sorted CD103$^+$CD56$^+$Lin$^-$ ILCs and CD103$^-$CD56$^+$Lin$^-$ ILCs from four primary high-grade serous tumors (OV225, OV332, OV738, and OV744; **A–D**). **A,** Heatmap of CD56$^+$Lin$^-$ ILC subsets with *z*-score of all differentially expressed genes. **B,** Volcano plot showing gene expression differences, summarized as $\log_2$ (FC) by $\log_{10}$ *P* value, between CD103$^+$CD56$^+$Lin$^-$ ILCs vs. CD103$^-$CD56$^+$Lin$^-$ ILCs. **C,** Normalized enrichment score (NES), FDR-adjusted *P* values, and gene counts are displayed for select gene sets that are upregulated or downregulated in CD103$^+$CD56$^+$Lin$^-$ ILCs compared with CD103$^-$CD56$^+$Lin$^-$ ILCs. **D,** Network clustering analysis using shared genes from gene sets significantly enriched in gene set enrichment analysis (GSEA) analysis of CD103$^+$CD56$^+$Lin$^-$ ILCs compared with CD103$^-$CD56$^+$Lin$^-$ ILCs. Gene sets with FDR-adjusted *P* values of ≤0.15 were included. All gene set clusters with at least five gene sets are displayed in terms of NES, gene set size, and similarity coefficient (measuring gene overlap between two gene sets). ECM, extracellular matrix; EFP, estrogen-responsive finger protein; ER, endoplasmic reticulum; MMP, matrix metalloproteinase; MPR, mannose phosphate receptor; PDGFRβ, platelet-derived growth factor receptor beta; ROS, reactive oxygen species; TPO, thrombopoietin.

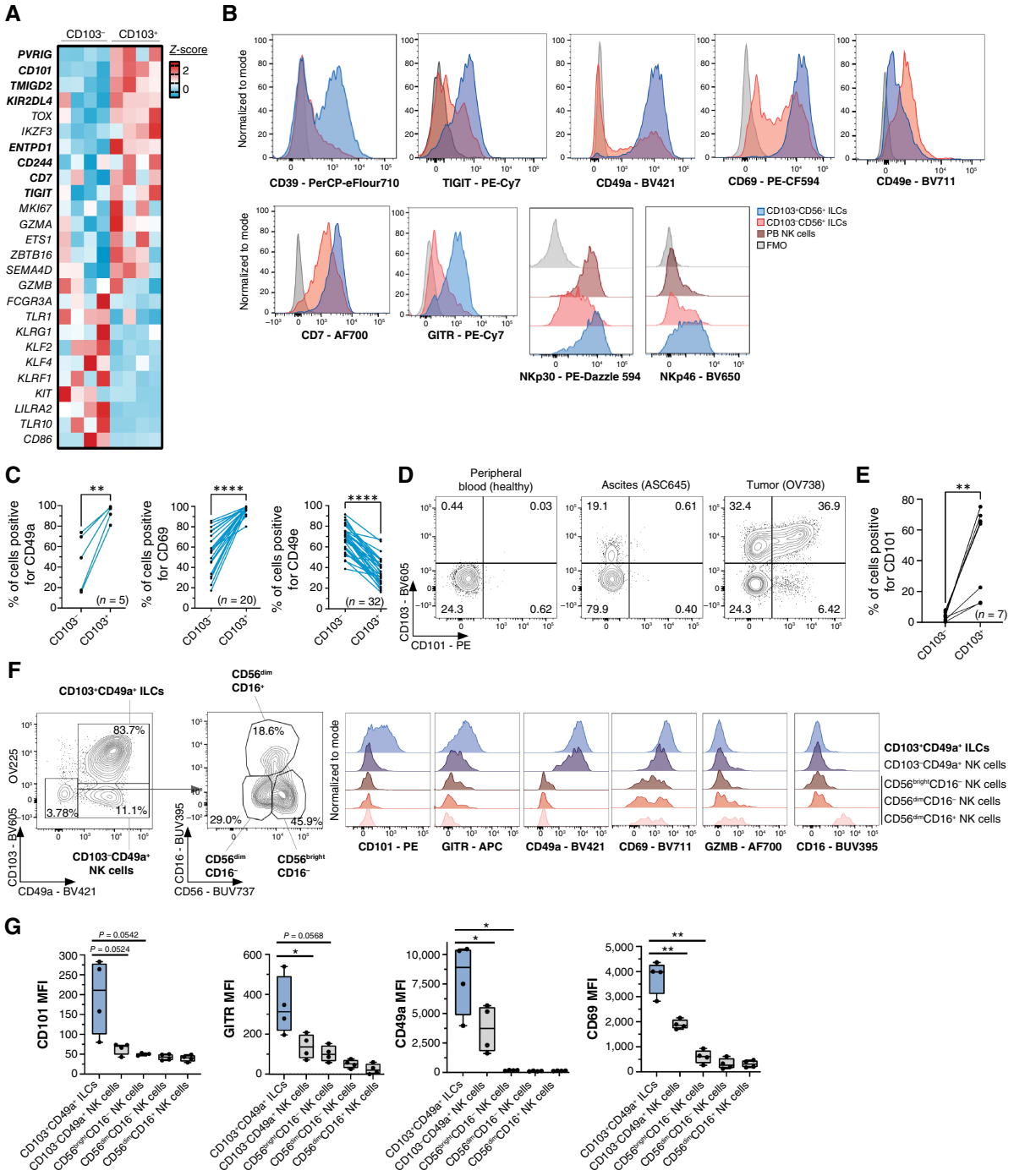

Figure 3.

CD103⁺CD56⁺Lin⁻ ILCs express CD101 and are phenotypically distinct from other CD56⁺ ILC subsets. **A,** Heatmap from bulk RNA-seq of FACS-sorted intratumoral CD103⁺CD56⁺Lin⁻ ILCs ($n = 4$) and CD103⁻CD56⁺Lin⁻ ILCs ($n = 4$) showing gene expression of immune molecules. Bolded text indicates markers previously associated with ILCs or that are inhibitory immune molecules. **B,** Flow cytometry staining of intratumoral CD56⁺Lin⁻ ILCs. Representative histograms showing surface expression of different markers between CD103⁺CD56⁺Lin⁻ ILCs and CD103⁻CD56⁺Lin⁻ NK cells. **C,** Summary dot plots of (**B**) with pairwise comparisons using a Student *t* test. **D,** Contour plots of CD56⁺Lin⁻ ILCs from peripheral blood (PB) of healthy donor, ascites, or tumor showing CD101 and CD103 expression. **E,** Summary dot plot of (**D**) with a paired Student *t* test. **F** (left), Contour plot gated on CD56⁺Lin⁻ ILC subsets including CD49a⁺CD103⁻ NK cells, CD56^{bright}CD16⁻ NK cells, and CD56^{dim}CD16$^{+/-}$ NK cells. Representative data from $n = 3$ tumors are shown. **F** (right), Histograms showing expression of various surface markers on CD103⁺CD49a⁺CD56⁺Lin⁻ ILCs compared with different NK cell subsets. **G,** Summary bar plots of (**F**). *, $P < 0.05$; **, $P < 0.01$; ****, $P < 0.0001$. FMO, fluorescence minus one; MFI, mean fluorescence intensity.

using an NKp46-dependent mechanism (32). In summary, intratumoral CD103$^+$CD56$^+$ ILCs are transcriptomically distinct from CD103$^-$CD56$^+$ ILCs, expressing increased features of tissue residency and molecules such as CD7, GITR, NKp30, and NKp46, which have been reported in inhibitory NK/ILC populations associated with the TME.

A marker that we had not expected to find to be enriched in CD103$^+$CD56$^+$ ILCs was *CD101* (**Fig. 3A**). CD101 is a member of the immunoglobulin superfamily and has been shown to be expressed on immunoregulatory cells [i.e., Tregs, CD8αα$^+$ regulatory T cells, and IL-10$^+$ dendritic cells (DC); Supplementary Fig. S3; refs. 81–85]. CD101^{high} Tregs have a higher suppressive capacity than CD101$^{dim/-}$ Tregs (81). Moreover, engagement of CD101 through agonist antibodies promoted human cutaneous DCs to suppress T cells through IL-10 (84). The increased gene expression of *CD101* in CD103$^+$CD56$^+$ ILCs (**Fig. 3A**), which we validated by flow cytometry (**Fig. 3D** and **E**), is consistent with an inhibitory role. Moreover, CD101, as well as GITR, distinguishes CD103$^+$CD56$^+$ ILCs from other NK cell subsets [including CD49a$^+$ NK cells (86), CD56^{bright} NK cells, and cytolytic CD56^{dim} NK cells; **Fig. 3F** and **G**; Supplementary Fig. S4A]. Although there has been limited evidence that CD101 is a marker for terminally differentiated cells with an exhausted state in LCMV models (87), these cells are likely not exhausted as CD101$^+$ cells within CD103$^+$CD56$^+$ ILCs had an increased expression of co-stimulatory molecule GITR and proliferation marker Ki67 compared with CD101$^-$ cells (Supplementary Fig. S4B and S4C). Overall, intratumoral CD103$^+$CD56$^+$ ILCs, but not other CD56$^+$ NK cell subsets, expressed CD101. Moreover, CD101$^+$CD103$^+$CD56$^+$ ILCs displayed an activated and proliferative state.

Intratumoral CD103$^+$CD56$^+$ ILCs have distinct transcriptional regulons and gene programs

We performed scRNA-seq to further characterize the CD103$^+$CD56$^+$ ILCs in the TME. First, we generated scRNA-seq data from a mixture of intratumoral CD45$^+$ and CD45$^-$ cells (1:1), resulting in 23 populations from unsupervised clustering (**Fig. 4A**; Supplementary Fig. S5, Supplementary Table S5 and S6). The CD56$^+$ (*NCAM1*) clusters (including clusters 10a and 10b) had higher expression of killer Ig–like receptors (i.e., *KIR2DL1*, *KIR2DL3*, *KIR2DL4*, *KIR3DL1*, and *KIR3DL2*), natural cytotoxicity receptors (i.e., *NCR1* and *NCR3*), and killer cell lectin–like receptors (i.e., *KLRF1*, *KLRD1*, *KLRC2*, *KLRK1*, *KLRC1*, *KLRC3*, *KLRG1*, and *KLRB1*), suggesting that they are CD56$^+$ ILCs (Supplementary Fig. S5D). When we applied unsupervised clustering on the CD56$^+$ ILC cluster, two populations were found and distinguished by the presence or absence of CD103 (*ITGAE*; **Fig. 4A**; Supplementary Fig. S5B).

SCENIC reconstructs gene regulatory networks through cis-regulatory motif analyses and infers TFs and cellular states at a single-cell level *in silico* (55). CD103$^+$CD56$^+$ ILCs showed enrichment of TF regulatory networks associated with development, differentiation, and function of group 1 ILCs (i.e., *NFIL3*, *RUNX3*, *GATA3*, and *BACH2*; **Fig. 4B**; Supplementary Fig. S6; Supplementary Table S7; refs. 88, 89). For example, BACH2 acts as a negative regulator of NK cell maturation and inhibits cytolytic programming (88). RUNX3 is essential for normal development and survival of ILC1s (90) and programs CD8$^+$ T-cell residency in non-lymphoid tissues and tumors (91). Regulons involved in RUNX3-dependent transcriptional circuitry including interferon regulatory factor 4 (*IRF4*) and *PRDM1* (92) were also enriched in CD103$^+$CD56$^+$ ILCs. The increased protein expression of IRF4 was validated with flow cytometry (**Fig. 4C**). It was also observed that Retinoid X receptor alpha (*RXRA*) regulon, a nuclear receptor activated by retinoic acid, was enriched in CD103$^+$CD56$^+$ ILCs. Retinoic acid has been shown to induce IL-10–expressing inhibitory ILC2s (93) and modulate Treg differentiation from naïve CD4$^+$ T cells (94). These findings suggest a distinct TF circuitry in intratumoral CD103$^+$CD56$^+$ ILCs compared with CD103$^-$CD56$^+$ NK cells.

To complement the SCENIC analysis, we investigated differences in TFs that are often defined in ILCs in the intratumoral CD103$^+$CD56$^+$ ILCs in contrast to CD103$^-$CD56$^+$ NK cells (Supplementary Fig. S7). ILC subsets are often defined by expression of the TFs TBET, EOMES, and RORC (Supplementary Fig. S1A and S1B; ref. 95). Although there was a trend toward a reduced level of TBET, CD103$^+$CD56$^+$ ILCs did not show a significant difference in protein expression of EOMES, compared with CD103$^-$CD56$^+$ ILCs. Although SCENIC analysis showed an enrichment of *GATA3*, *RORC*, and *FOXP3* regulons, we did not observe expression of these proteins by flow cytometry (Supplementary Fig. S7). However, CD103$^+$CD56$^+$ ILCs upregulated gene expression of TFs related to FOXP3-associated complexes (i.e., *ETS1* and *IKZF3*) and ILC development (i.e., *TOX* and *ZBTB16*; **Fig. 3A**). ETS1 (ETS proto-oncogene 1) interacts with FOXP3 intronic enhancer, which is required for Treg development and suppressive functions (96). Enrichment of TOX and PLZF (*ZBTB16*) were further confirmed by flow cytometry (Supplementary Fig. S7A and S7B). PLZF identifies CD8αα$^+$ T cells that control T cell–mediated autoimmunity through perforin (97). Although intratumoral CD103$^+$CD56$^+$ ILCs did not express detectable levels of FOXP3 (Supplementary Fig. S7D and S7E), they expressed a subset of genes that overlap with those expressed by Tregs (**Fig. 4D**; refs. 35, 81, 84, 88, 96, 98–111). In contrast, CD103$^-$CD56$^+$ NK cells expressed gene signatures more similar to γδ T cells, which may be because of shared innate cytotoxicity mechanisms. Overall, these findings suggest that intratumoral CD103$^+$CD56$^+$ ILCs express unique gene programs.

Several groups have identified other ILC subsets within the CD56$^+$ populations, including CD56$^+$ ILC3s and CD56$^+$ intraepithelial ILC1s within the tonsil (66, 67, 112). To determine whether CD103$^+$CD56$^+$ ILCs shared features with other ILC subtypes, we performed cellular indexing of transcriptomes and epitopes sequencing on sorted CD45$^+$Lin$^-$CD56$^+$ ILCs mixed with CD45$^+$Lin$^-$CD127$^+$ ILCs in a 1:1 ratio for three additional ovarian tumors to enrich for ILCs and ensure sufficient cell numbers for analysis. After batch-correction and preprocessing *in silico*, 4,703 genes and 134 protein markers were utilized for unsupervised clustering, which resulted in five clusters identifying ILCs (**Fig. 4E–G**; Supplementary Tables S5 and S6). Gating on the protein expression of CD56$^+$CD3$^-$ cells, we found that they clustered mostly with NK cells (39.11%), CD103$^+$ILCs (35.02%), ILC3s (19.46%), ILC1s (4.28%), and ILC2s (2.14%; **Fig. 4F**; Supplementary Fig. S8A and S8B). The CD56$^+$CD3$^-$ cells that express protein levels of both CD103 and CD49a were mostly specific to cluster 0 (Supplementary Fig. S8C and S8D). Although there were some ILC3s (cluster 3) and *Ki67*$^+$ ILC1s (cluster 5) that expressed CD56, these cells did not express CD103. CD103$^+$CD56$^+$ ILCs did not express markers related to conventional NK cells (i.e., CD16, CD57, CD45RA, KIR2DL2, KIR3DL1, and *KLRF4*) or ILC3-related markers (i.e., cKit, ICOS, and CD25; Supplementary Fig. S9A and S9B). Similarly, markers associated with tonsillar CD56$^+$ ILC3s characterized by Cella and colleagues (66) were not expressed by CD103$^+$-CD56$^+$ ILCs (i.e., *IL1R1*, *IL23R*, *IL7R*, *CCL20*, *CD33*, *CSF2*, *FXYD5*, *NCR2*, *NFKBIA*, *PRR5*, *RORC*, *TNFSF13B*, and *TOX2*; Supplementary Fig. S9C). Therefore, there is no evidence to support that these

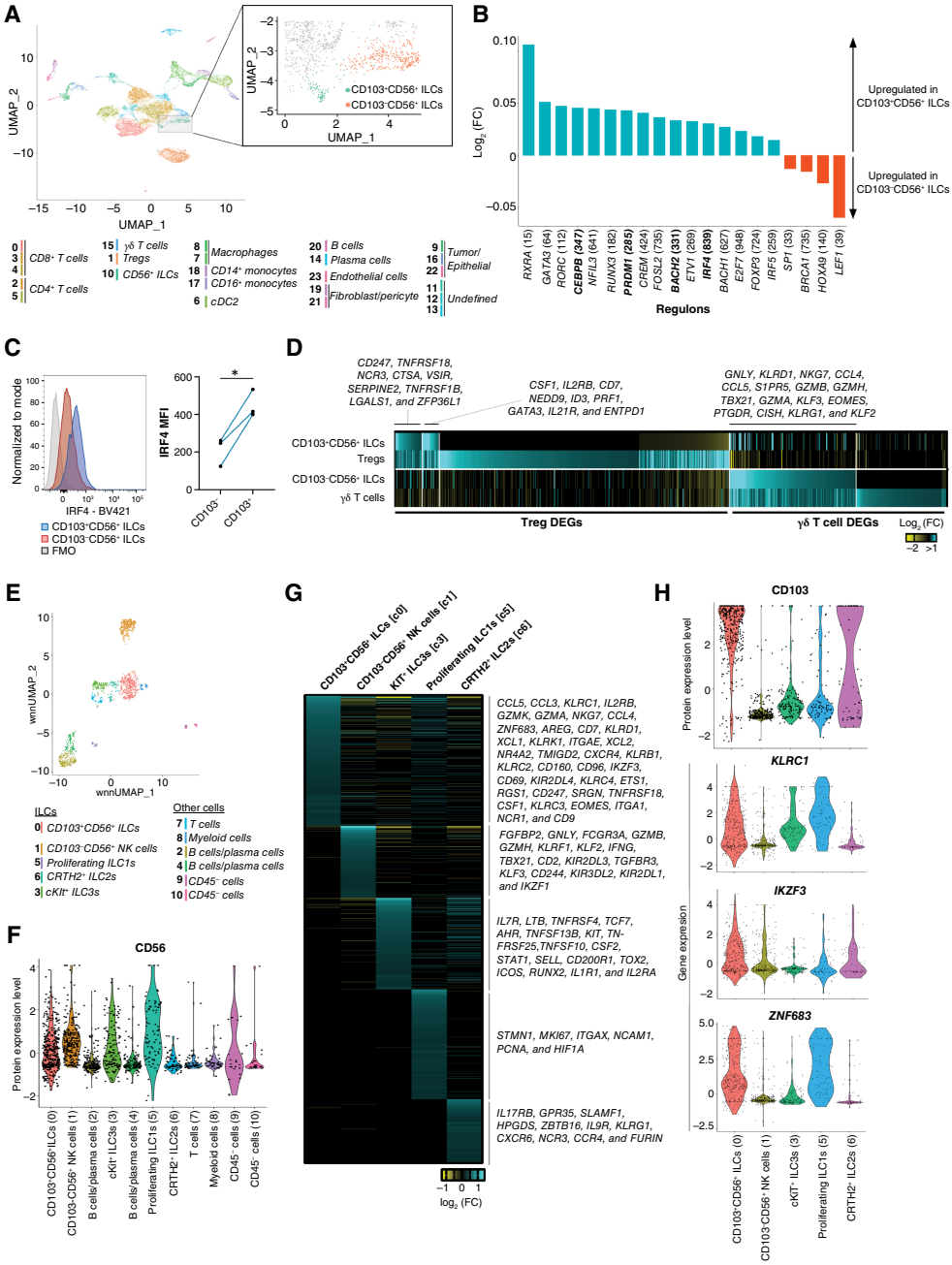

Figure 4.

scRNA-seq reveals distinct transcriptional regulons and gene programs in intratumoral CD103^{+}CD56^{+} ILCs. scRNA-seq was performed on FACS-sorted CD45^{+} immune cells and CD45^{-} non-immune cells mixed in 1:1 ratio from three primary high-grade serous tumors (OV348, OV744, and OV749). A total of 15,742 cells successfully passed quality control and were included in this analysis. **A,** UMAP color coded by population, with CD56^{+} ILCs highlighted (right) and reanalyzed with unsupervised clustering into two subsets: CD103^{+}CD56^{+} ILCs ($n = 90$) and CD103^{-}CD56^{+} ILCs ($n = 334$). CD56^{+} ILCs with new subclusters were pooled back into original UMAP for comparisons across other immune cell types (right). **B,** SCENIC was performed to infer TF networks that are upregulated in CD103^{+}CD56^{+} ILCs compared with CD103^{-}CD56^{+} ILCs. Regulons that had an adjusted *P* value <0.01 are shown. Numerical values in brackets indicate the number of genes associated with each regulon. Regulons labeled in blue have previously been shown to have roles in Treg development, differentiation, and suppressive functions. **C,** Histogram (left) and summary dot plot with a paired Student *t* test (right) of IRF4 staining by flow cytometry. **D,** Heatmap comparing Treg DEGs or γδ T-cell DEGs by $\log_2$ (FC) that reached adjusted *P* value <0.01 in different populations of cells (i.e., CD103+CD56+ ILCs, Tregs, CD103^{-}CD56^{+} ILCs, and γδ T cells). Cellular indexing of transcriptomes and epitopes sequencing (CITE-seq) of intratumoral CD56^{+}CD127$^{+/-}$Lin^{-} (CD3^{-}TCRαβ^{-}TCRγδ^{-}CD14^{-}CD19^{-}CD20^{-}CD34^{-}CD123^{-}CD303^{-}FcεRIα^{-}) ILCs and CD56^{-}CD127^{+}Lin^{-} ILCs mixed in a 1:1 ratio from primary ovarian tumors (**E–H**). **E,** UMAP of unsupervised clustering resulting in five ILC subsets (*c0*, *c1*, *c3*, *c5*, and *c6*). **F,** Protein expression of CD56 across all cells and CD103 across all ILC subsets. **G,** Heatmap of genes differentially expressed within each ILC cluster showing $\log_2$ (FC). **H,** Violin plots of protein expression CD103 or gene expression of *KLRC1*, *IKZF3*, and *ZNF683*. *, $P < 0.05$. DEG, differentially expressed genes; FC, fold change; FMO, fluorescence minus one; MFI, mean fluorescence intensity.

$CD103^+CD56^+$ ILCs are related to the $CD56^+$ ILC3 subset. Currently, there are no clear markers that can distinguish tissue-resident NK cells and $CD56^+$ ieILC1s in human tissues (4). Although $CD103^+CD56^+$ ILCs also expressed various markers associated with group 1 ILCs (i.e., *KLRB1*, *KLRD1*, and *KLRC3*), $CD103^-CD56^+$ NK cells and *Ki67*$^+$ ILC1s also expressed these genes (Supplementary Fig. S9C). In contrast to $CD103^-CD56^+$ NK cells, both $CD103^+CD56^+$ ILCs and *Ki67*$^+$ ILC1s expressed *KLRC1* and *ZNF683* (encoding protein Hobit; **Fig. 4H**). Hobit is a key TF that regulates tissue residency and differentiation in murine tissue–resident NK cells and ILC1s, but the requirement of these cells for Hobit varies in different tissues (113, 114). $CD103^+CD56^+$ ILCs were distinct from *Ki67*$^+$ ILC1s because of their expression of TF *IKZF3* (encoding protein Aiolos; **Fig. 4H**) and the absence of CD27 and CD71 (Supplementary Fig. S9D). Finally, we did not find evidence that $CD103^+CD56^+$ ILCs were composed of heterogeneous populations. Subclustering of these cells *in silico* resulted in two subclusters that did not have many genes that were differentially expressed (Supplementary Fig. S9D and S9E; Supplementary Table S6). It is possible that these subclusters represent differences in the cellular state, such as activation status, rather than representing different ILC subsets. Overall, $CD103^+CD56^+$ ILCs isolated from ovarian cancer represent a distinct population of cells that have unique transcriptomic programs.

$CD103^+CD56^+$ ILCs are associated with $CD8^+$ T cells that express low levels of GZMB within the TME

To determine whether $CD103^+CD56^+$ ILCs affect $CD8^+$ T cells, we cocultured sorted $CD45^+$ immune cells from surgically resected tumors ($n = 4$) with soluble anti-CD3s with or without intratumoral $CD103^+CD56^+$ ILCs in a 1:3 or 1:5 ratio (suppressor: all other $CD45^+$ immune cells; **Fig. 5A**). These assays were done using samples from four patients across two experiments in which the analyses were kept separately. $CD8^+$ TILs cultured with intratumoral $CD103^+CD56^+$ ILCs showed reduced expression of cytolytic molecule GZMB (**Fig. 5B** and **C**). Moreover, when intratumoral $CD103^+CD49a^+CD56^+$ ILCs were cultured with T cells and soluble anti-CD3 and anti-CD28 (**Fig. 5D**), $CD8^+$ T cells had a reduced expression of activation marker CD25 and reduced proportion of $CD25^+GZMB^+CD8^+$ T cells (**Fig. 5E** and **F**). The proliferation marker Ki67 was also reduced in $CD8^+$ T cells when cultured with $CD103^+CD49a^+CD56^+$ ILCs (**Fig. 5G**). These findings suggest that intratumoral $CD103^+CD49a^+CD56^+$ ILCs may inhibit $CD8^+$ T-cell effector function.

To examine whether $CD103^+CD56^+$ ILCs were associated with a similar $CD8^+GZMB^{lo}$ phenotype *ex vivo*, we characterized intratumoral T cells from patients with varying proportions of $CD103^+CD56^+$ ILCs (**Fig. 6A**). It is important to note that there was interpatient heterogeneity in the proportion of $CD103^+CD56^+$ ILCs present within the TME (Supplementary Fig. S10A). We found that $CD103^+CD56^+$ ILC^{high} tumors correlated with a reduction in GZMB-expressing $CD8^+$ T cells (**Fig. 6A**), consistent with the ILC coculture assays above. Similar findings were observed when we evaluated GZMB expression in $CD8^+$ T cells from samples with high proportions of $CD103^+CD56^+$ ILCs (ILC^{high}; >60% of $CD56^+$ ILCs positive for CD103) compared with low proportions of $CD103^+CD56^+$ ILCs (ILC^{low}; <40% of $CD56^+$ ILCs positive for CD103; **Fig. 6B**). Similarly, linear regression analysis showed that as tumors had an increasing proportion of $CD103^+CD56^+$ ILCs, there was a decrease in GZMB-expressing $CD8^+$ T cells (**Fig. 6C**). Duhen and colleagues (115) and others have previously found that $CD39^+CD103^+$ cells are enriched for tumor-reactive T cells in human solid tumors (116). Therefore, we examined whether antigen-specific $CD8^+$ T cells were present and whether they correlated with the proportion of $CD103^+CD56^+$ cells (Supplementary Fig. S10B–S10D). The presence of $CD103^+CD56^+$ ILCs was associated with high abundance of potentially antigen-specific $CD39^+CD103^+CD8^+$ T cells (Supplementary Fig. S10C) despite our findings that there were reduced proportions of GZMB-expressing $CD8^+$ T cells (**Fig. 6A–C**). Similarly, patients with the $CD103^+CD56^+$ ILC^{high} group had a trend toward increased proportion of $CD39^+CD103^+CD8^+$ T cells (Supplementary Fig. S10B). Linear regression analysis showed that as tumors had an increasing proportion of $CD103^+CD56^+$ ILCs, there was also an increase in $CD39^+CD103^+$ $CD8^+$ T cells (Supplementary Fig. S10D). Therefore, our data are consistent with the interpretation that the presence of $CD103^+CD56^+$ ILCs correlate with the downregulation of GZMB on potentially antigen-specific cytotoxic T cells found in the same TME.

To determine whether these $CD103^+$ inhibitory ILCs were physically interacting with T cells within the tumor, we performed IMC on formalin-fixed, paraffin-embedded slides from HGSC tumors (**Fig. 6D**). NKp46 was used to identify $CD103^+$ ILCs as CD56 expression is highly abundant in ovarian tumor cells and identifying these ILCs from background through histology approaches with CD56 is not feasible. Moreover, NKp46 is expressed on the majority of $CD103^+CD56^+$ ILCs (**Fig. 3E**). We found that the $CD8^+$ T cells in contact with $CD103^+NKp46^+Lin^-$ ILCs had a lower expression of GZMB and Ki-67 compared with $CD8^+$ T cells not in contact with these ILCs (**Fig. 6E** and **F**). To determine other lymphocytes that interacted with $CD103^+NKp46^+Lin^-$ ILCs, we plotted $CD45^+$ immune cells that were in contact with $CD103^+NKp46^+Lin^-$ ILCs on an UMAP and identified cell clusters after unsupervised clustering (**Fig. 6G** and **H**; Supplementary Fig. S10E and S10F). Among all the cells that came into contact with $CD103^+NKp46^+Lin^-$ ILCs, we found that they were preferentially in contact with $GZMB^{low}CD8^+$ T cells compared with other cell subsets (**Fig. 6I**). Overall, our findings suggest that $CD103^+$ ILCs are interacting with T cells with a lower cytolytic potential in the TME, providing a direct association between *ex vivo* findings and our *in vitro* cultures.

To further investigate the association between $CD103^+CD56^+$ ILCs with altered an $CD8^+$ T-cell profile, we performed scRNA-seq of intratumoral $CD45^+Lin^+$ cells. First, we characterized three subsets of intratumoral $CD8^+$ T cells (**Fig. 7A**; Supplementary Table S5 and S6) and performed differentially expressed gene analysis for each subset (c1, c2, and c9) comparing $CD8^+$ T cells from tumors with high proportions of $CD103^+CD56^+$ ILCs [i.e., OV710 (*80.4%*) and OV348 (*93.4%*)] compared with tumors with lower proportions of $CD103^+CD56^+$ ILCs [i.e., OV749 (*4.6%*); OV744 (*9.4%*); and OV702 (*40.9%*); **Fig. 7B**; Supplementary Table S8]. $CD8^+$ T cells from $CD103^+CD56^+$ ILC–high tumors had a lower expression of genes within T-cell receptor (TCR) signaling pathway (e.g., *CD3G*, *CD8B*, *CD247*, *IKBKB*, *LAT*, *MAPK3*, *NFATC4*, *PAK4*, *PPP3CB*, *RASA1*, *SHC*, *SOS1*, *VAV3*, and *ZAP70*) compared with cells from $CD103^+CD56^+$ ILC–low tumors (**Fig. 7C**). To identify genes associated with T-cell activation, we performed scRNA-seq of $CD8^+$ T cells from healthy donor peripheral blood mononuclear cells and stimulated them with anti-CD3 and anti-CD28 for 18 hours *in vitro* and identified a T-cell activation signature. Surprisingly, intratumoral $CD8^+$ T cells in $CD103^+CD56^+$ ILC–high tumors had a lower expression of genes that were involved in T-cell activation (e.g., *CD38*, *CD47*, *CDK4*, *CISH*, *FASLG*, *IL2RA*, *IL2RB*, *IKZF4*, *PTPN6*, *TIGIT*, *TNFRSF4*, *STAT1*, and *STAT2*) compared with cells from $CD103^+CD56^+$ ILC–low tumors (**Fig. 7D**). Overall,

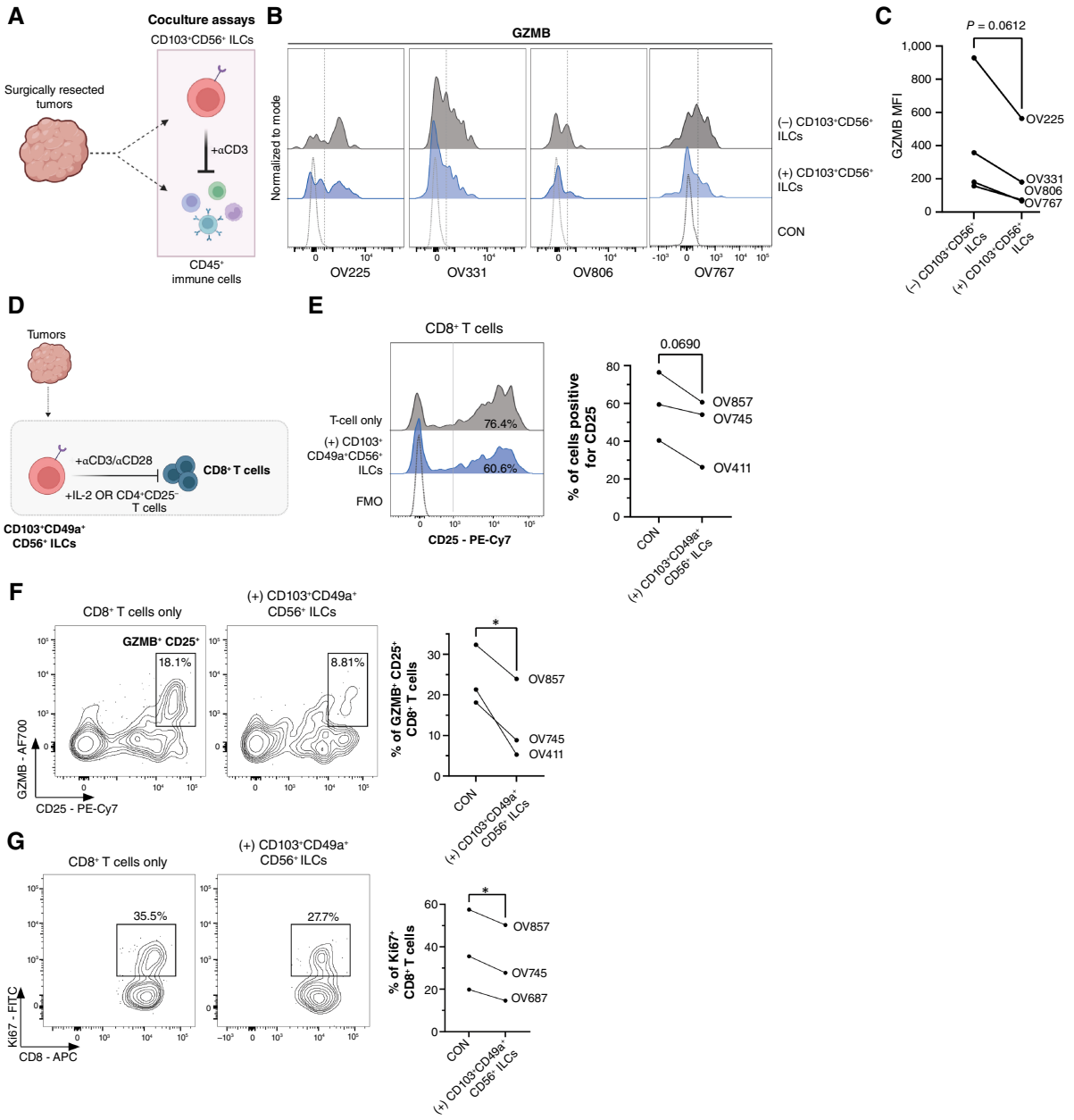

Figure 5.

Intratumoral CD103⁺CD56⁺Lin⁻ ILCs alter autologous CD8⁺ T-cell phenotypes. **A,** Schematic diagram of coculture assays in which intratumoral CD45⁺ TILs were FACS sorted from four patients with HGSC (OV225, OV331, OV767, and OV806) and cocultured with autologous intratumoral CD103⁺CD56⁺Lin⁻ (CD3⁻CD14⁻CD19⁻) ILCs at a 1:3 or 1:5 ratio (suppressor : responders) with soluble αCD3 monoclonal antibodies for 4 days. CD8⁺ TILs in conditions with or without intratumoral CD103⁺CD56⁺Lin⁻ ILCs were measured for expression of GZMB (**B** and **C**). These assays have two to seven technical replicates, and samples were conducted over two separate experiments (i.e., left to right: OV225, OV331, and OV806; OV767; **B**). **D,** Schematic diagram of coculture assays in which intratumoral CD8⁺ T cells were FACS sorted from four patients with HGSC (OV411, OV687, OV745, and OV857) and cocultured with autologous intratumoral CD103⁺CD49a⁺CD56⁺Lin⁻ ILCs with αCD3/αCD28 monoclonal antibodies for 4 days. OV411, OV745, and OV857 were cultured at a 1:1 ratio (suppressor : responder) with 15,000 T cells, whereas OV687 was cultured in a 1:13 ratio with 10,000 T cells. To provide additional support to increase survival of CD8⁺ T cells in culture, IL-2 (100 IU; i.e., OV745, OV411, and OV687) or CD25⁻CD4⁺ T cells (i.e., OV857) were added to the cultures. **E,** Expression of CD25 in CD8⁺ T cells with or without coculture of CD103⁺CD49a⁺CD56⁺Lin⁻ ILCs are shown as histograms (left) or pairwise comparisons (right). Proportion of GZMB⁺CD25⁺ CD8⁺ T cells (**F**) or Ki67⁺CD8⁺ T cells (**G**) are shown as contour plots (left) or pairwise comparisons (right). Ki67⁺, GZMB⁺ KI67⁺, or GZMB⁺CD25⁺ CD8⁺ T cells from co-cultures are shown as contour plots (**F**) or pairwise comparisons (**G**). **C** and **E–G,** Pairwise two-tailed Student *t* tests were used as statistical tests and lines corresponding to cells from the same patient are shown. *, $P < 0.05$. CON, FMO staining control; FMO, fluorescence minus one; MFI, mean fluorescence intensity. (Schematics in **A** and **D** were created with BioRender.com.)

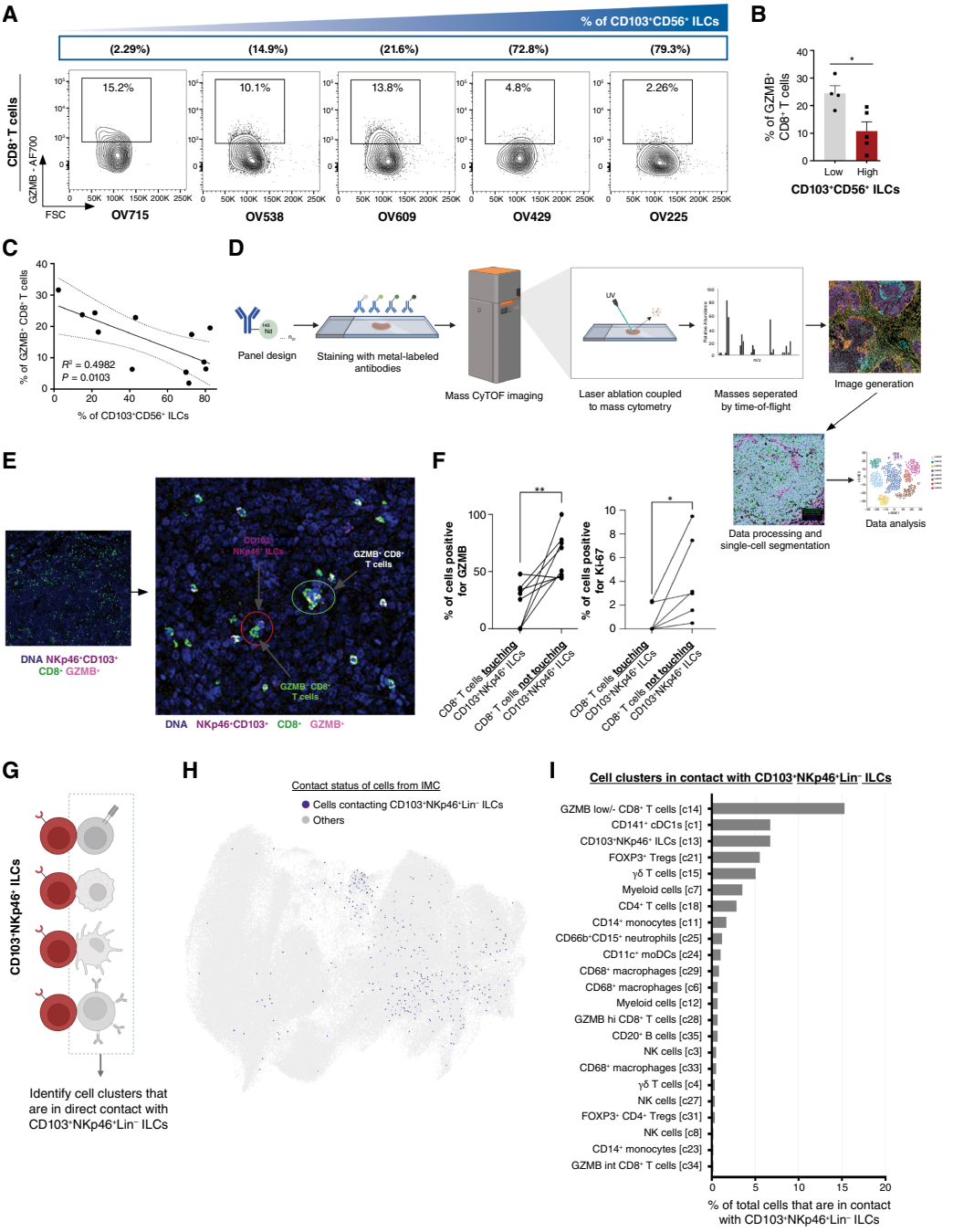

Figure 6.

CD103$^+$CD56$^+$Lin$^-$ ILCs are associated with CD8$^+$ T cells that express lower levels of GZMB within the TME. To evaluate the phenotype associated with CD103$^+$CD56$^+$ ILCs, flow cytometry was used to characterize CD8$^+$ T cells with varying proportions of CD103$^+$CD56$^+$Lin$^-$ ILCs (**A–C**). Intracellular expression of GZMB is shown on CD8 cells (**A**), with five different tumor fragments from patients with HGSC displayed with increasing proportions of CD103$^+$CD56$^+$Lin$^-$ ILCs (from left to right). **B,** T-cell profiles from patients that have a high abundance of CD103$^+$CD56$^+$Lin$^-$ ILCs (>75%, $n = 5$) or low abundance of CD103$^+$CD56$^+$Lin$^-$ ILCs (<25%, $n = 4$). An unpaired two-tailed Student *t* test was performed. **C,** Linear regression of intratumoral T-cell expression of GZMB is shown with proportion of CD103$^+$CD56$^+$Lin$^-$ ILCs within the TME ($n = 12$). **D,** IMC was performed on eight HGSC tumors to identify cells that were physically interacting with CD103$^+$NKp46$^+$Lin$^-$ ILCs *in situ*. **E,** Representative image of CD103$^+$Nkp46$^+$Lin$^-$ (PanCK-SMA-Vim-CD3$^-$CD20$^-$CD14$^-$CD15$^-$CD16$^-$CD123$^-$CD127$^-$CD117$^-$) cells (*labeled in purple*) interacting with GZMB-CD8$^+$ T cells (*labeled in green*). **F,** The percentage of CD8$^+$ T cells expressing GZMB or Ki-67 that were either (i) touching CD103$^+$NKp46$^+$Lin$^-$ ILCs or (ii) not touching CD103$^+$NKp46$^+$Lin$^-$ ILCs are shown on dot plots. Lines show paired tumor samples. To determine other cell types that interacted with CD103$^+$NKp46$^+$Lin$^-$ ILCs (**G**), we isolated these contacting cells *in silico* and identified the cell type classification (**H**). **I,** From the total of cells in contact with CD103$^+$Nkp46$^+$Lin$^-$ ILCs, the total proportion of these cells that belonged to each cell cluster is shown in a bar graph. Cells from undefined cell clusters were not shown and excluded from analysis. *, $P < 0.05$; **, $P < 0.01$; variance displayed as SEM. CyTOF, cytometry time-of-flight; FSC, forward scatter. (Schematics in **D** and **G** were created with BioRender.com.)

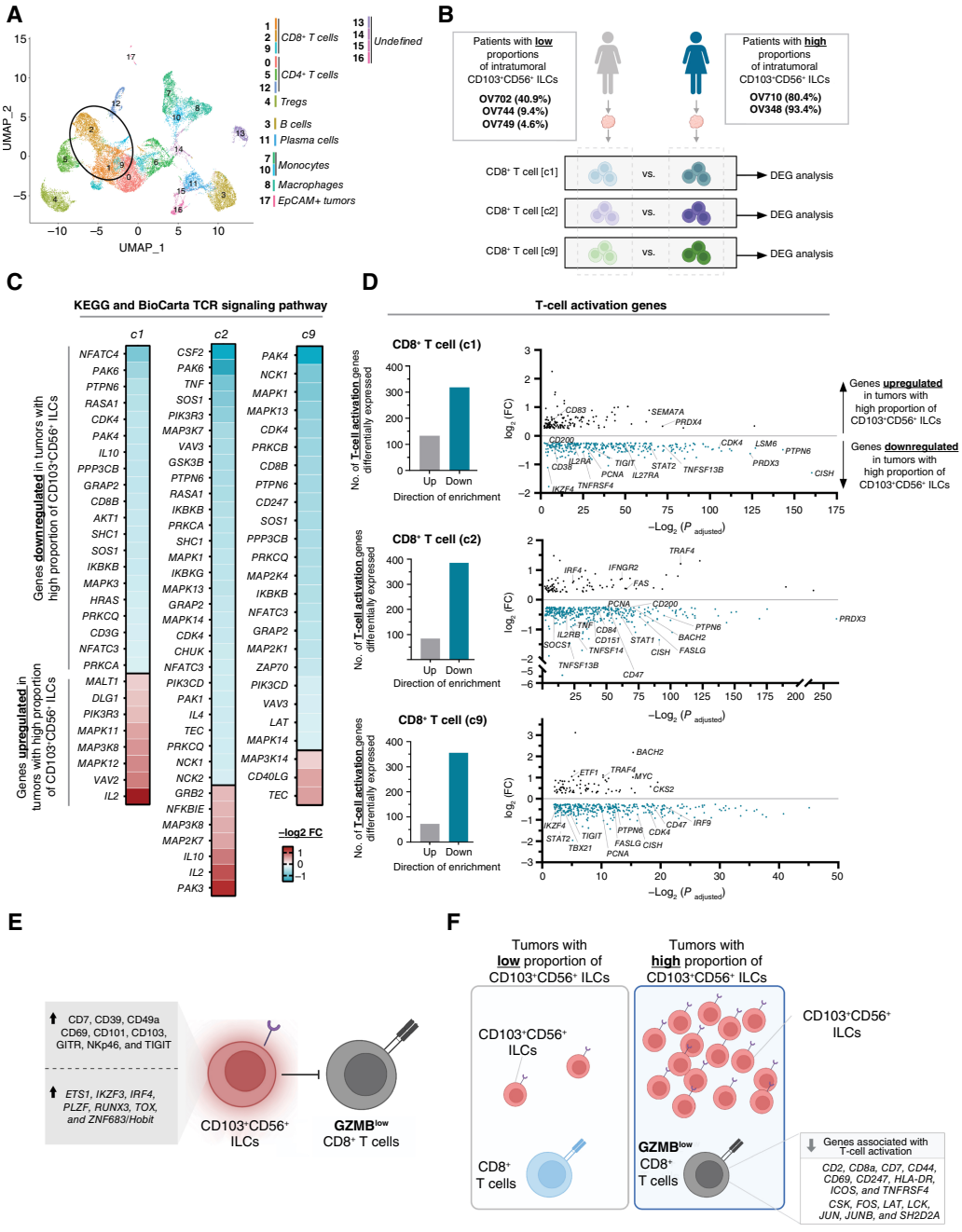

Figure 7.

CD103⁺CD56⁺Lin⁻ ILCs are associated with CD8⁺ T cells with a reduced activated transcriptomic signature. **A,** scRNA-seq was performed on FACS-sorted CD45⁺ immune cells with removal of CD56⁺Lin⁻ ILCs from six primary ovarian tumors and unsupervised clustering resulted in 17 clusters. **B,** CD8⁺ T cells from tumors with high proportions of CD103⁺CD56⁺ ILCs (i.e., OV710 and OV348) were compared with CD8⁺ T cells from tumors with low proportions of CD103⁺CD56⁺ ILCs (i.e., OV702, OV744, and OV749) and DEG analysis was performed. **C,** All genes that were differentially expressed and met the cutoff of $P_{adjusted}$ < 0.01 and log_2 FC > 0.25 that belonged to the KEGG T-cell receptor signaling pathway and the Biocarta TCR pathway are shown as a heatmap of log_2 FC for each CD8⁺ T cell clusters (c1, c2, and c9). To develop a T-cell activation gene signature, we performed scRNA-seq of CD8⁺ T cells from peripheral blood mononuclear cells of healthy donors activated with αCD3/αCD28 for 18 hours. **D** (left), Total number of T-cell activation genes that were upregulated or downregulated in intratumoral CD8⁺ T cells from (**A**) and (**B**) in CD103⁺CD56⁺ ILC–high tumors compared with CD103⁺CD56⁺ ILC–low tumors. **D** (right), Dot plot in which each dot represents genes within the T-cell activation gene signature that were differentially expressed between CD8⁺ T cells from CD103⁺CD56⁺ ILC–high tumors compared with CD103⁺CD56⁺ ILC–low tumors and reached significance thresholds ($P_{adjusted}$ < 0.01 and log_2 FC > 0.25). **E** and **F,** Schematics showing that CD103⁺CD56⁺ ILCs are associated with an altered CD8⁺ T-cell profile. DEG, differentially expressed genes; FC, fold change; KEGG, Kyoto Encyclopedia of Genes and Genomes; No., number. (Schematics in **B**, **E**, and **F** were created with BioRender.com.)

$CD103^+CD56^+$ ILCs are associated with $CD8^+$ T cells with less cytotoxic capacity and reduced activation status.

Discussion

In this study, we have examined the cellular composition of the ovarian TME with the goal to identify intratumoral ILCs that have given rise to the inhibitory population originally identified in TIL cultures (32). We have found that the expression of CD103 delineated $CD56^+$ ILCs that were associated with poor proliferative capacity of TILs in culture. We characterized $CD103^+CD56^+$ ILCs directly from the TME and found that they expressed distinct features and transcriptional regulons. $CD103^+CD56^+$ ILCs were able to reduce the expression of the cytolytic molecule GZMB on autologous $CD8^+$ T cells *in vitro*. Moreover, $CD8^+$ T cells found in the same TME with $CD103^+CD56^+$ ILCs also showed a reduced GZMB expression and had a transcriptional signature consistent with a less activated phenotype. Using IMC, we further showed evidence for a direct interaction of these cells *in situ*. Collectively, the presence of $CD103^+CD56^+$ ILCs correlated with $GZMB^{low}CD8^+$ T cells, suggesting that tumors with a prominent population of $CD103^+CD56^+$ ILCs would show limited immunosurveillance and poor prognosis.

Group 1 ILCs expressing tissue retention molecules (i.e., CD103 and CD49a) have been shown to suppress T cells in chronic viral infection models (78, 117, 118) and may have tumor-promoting functions in cancer models (119, 120). Moreover, human $CD103^+$ group 1 ILCs induced *in vitro* have been previously demonstrated to suppress T cells. For example, Neo and colleagues (34) found that $CD73^+CD56^+$ ILCs from peripheral blood cocultured with tumor cells could subsequently suppress T-cell proliferation and reduce IFN-γ expression via IL-10. Although they did not characterize the expression of tissue retention proteins from ILCs directly from tumors, their supplementary table showed an increase in *ITGAE* (CD103) gene expression in $CD73^+$ peripheral blood cells cocultured with primary sarcoma tumors. Recently, our group has found that peripheral blood NK cells treated with TGF-β1 and IL-15 had an increased expression of CD103, CD49a, GITR, and CD101 (121) which have a similar expression profile as intratumoral $CD103^+CD56^+$ ILCs from ovarian cancer as described here. Moreover, TGF-β1/IL-15–induced $CD103^+CD56^+$ NK–like cells inhibited proliferation, reduced absolute numbers, and reduced CD25 expression of autologous T cells *in vitro* (121). In this current study, we found that $CD103^+CD56^+$ ILCs directly isolated from ovarian tumors downregulated the expression of activation marker CD25 and proliferation marker Ki67 on autologous $CD8^+$ T cells *in vitro*. We also found that $CD103^+CD56^+$ ILCs downregulated GZMB expression on $CD8^+$ T cells *in vitro* and were associated with $GZMB^{low}CD8^+$ T cells within the TME. Similarly, Tregs have also been shown to reduce effector functions and cytolytic activity in T cells (122–124). Although we were unable to clearly demonstrate that these $CD103^+CD56^+$ ILCs isolated directly from the tumors could inhibit proliferation of $CD4^+$ T cells or $CD8^+$ T cells because of the extremely low numbers of these cells within the TME, our analysis here, in combination with findings from our previous work with *in vitro*–generated $CD103^+CD56^+$ cells (121), is consistent with the possibility that these cells may acquire a regulatory function if they encountered appropriate signals in the TME and further develop into inhibitory cells. Collectively, these findings suggest that $CD103^+CD56^+$ ILCs from ovarian tumors have inhibitory properties.

It is important to note that the regulation of $CD8^+$ T cells by ILC1-like cells occurs in very defined conditions. Xu and colleagues (125, 126) and Crouse and colleagues (126) found that type I IFNs were required to render $CD8^+$ T cells susceptible to NK cell–mediated killing in LCMV-infected mice through a Qa-1/NKG2A-dependent mechanism (127). This suggests that the potential inhibitory role of $CD103^+CD56^+$ ILCs may differ according to the TME context and the ligands present on $CD8^+$ T cells. Moreno-Nieves and colleagues (128) described a population of $CD103^+CD49a^+CD56^+$ NK cells with an ieILC1-like signature in head and neck squamous cell carcinoma (HNSCC). Although they found that *in vitro*–induced $CD49a^+$ NK cells, derived from healthy peripheral blood NK cells stimulated with IL-15 and the HNSCC cell line PCI-33, showed potent antitumor activity against xenograft tumors, it is unclear whether intratumoral $CD103^+CD56^+$ NK cells directly isolated from HNSCC have an immune-inhibitory function. It is possible that NK cells and ILCs have various roles within the TME, and further studies are needed to investigate mechanisms that promote antitumor immunity or trigger an inhibitory function of ILCs.

Although previous studies have correlated $CD8^+$ T-cell infiltration with prognosis or survival, several studies have evaluated GZMB levels in the $CD8^+$ T cells as well. For example, IHC approaches have found that tumors with both low GZMB expression and low $CD8^+$ T-cell densities were associated with poor clinical outcomes in several cancers (129–131). Zhu and colleagues (132) found that low densities of $GZMB^+CD8^+$ T cells by IMC, indicating lower proportion of cytotoxic $CD8^+$ T cells, were associated with poor overall survival in patients with high-grade serous carcinomas. Patients with metastatic melanoma or triple-negative breast cancer that responded to anti-PD1/PDL1 single agent or combination therapy were associated with increased GZMB-expressing $CD8^+$ T cells (133–138). Recent studies have attempted to categorize tumors with functional markers expressed by $CD8^+$ T cells and found a correlation with a distinct TME subset (136, 139, 140). Using scRNA-seq, Tietscher and colleagues (140) identified a subset of patients with breast tumors that did not have $CD8^+$ T cells with a $PD\text{-}1^{high}CTLA\text{-}4^{high}CD38^{high}$–activated/exhausted phenotype and had a TME with innate and adaptive lymphocytes that expressed lower levels of cytolytic markers *GZMB*, *GNLY*, and *FASLG*. Moreover, these tumors were associated with myeloid cells with a reduced inflammatory and phagocytic phenotype. Gruosso and colleagues (141) also found that $GZMB^+CD8^+$ T cells identified using immunofluorescence were associated with more immunoreactive microenvironment with higher intratumoral type I IFN signature in patients with triple-negative breast cancer. These studies underscore the importance of understanding correlates and mechanisms that dictate different functional and dysfunctional profiles of $CD8^+$ T cells within the TME. One of the key findings in this current study is that $CD103^+CD56^+$ ILCs were associated with a reduction in GZMB-expressing $CD8^+$ T cells by flow cytometry and IMC. Moreover, scRNA-seq revealed that $CD103^+CD56^+$ ILCs were associated with $CD8^+$ T cells with a lower activation status. These findings suggest that $CD8^+$ T cells in tumors with a high abundance of $CD103^+CD56^+$ ILCs have a limited ability for immunosurveillance, possibly contributing to resistance to immunotherapy in patients with EOC (142).

In summary, we have identified intratumoral $CD103^+CD56^+$ ILCs that are associated with $CD8^+$ T cells with limited immune activity. Future work characterizing $CD103^+CD56^+$ ILCs, their mechanisms of activation, and whether they are associated with clinical outcomes across different cancers may lead to better understanding of the barriers for immunosurveillance, define new targets, and lead to improved treatment strategies.

Authors' Disclosures

H.W. Jackson reports grants, personal fees, and nonfinancial support from Standard BioTools, personal fees and nonfinancial support from Abcam, and nonfinancial support from Somalogic outside the submitted work. P.S Ohashi reports grants from Canadian Institutes of Health Research, Canadian Cancer Society, TRANSCAN3, and Princess Margaret Cancer Foundation Wolfond Immunotherapy Fund during the conduct of the study, as well as other support from Providence Therapeutics, Treadwell Therapeutics, Tikvo Allocell, and Rondo Therapeutics outside the submitted work. S.Q. Crome, P.S. Ohashi, and L.T. Nguyen filed a patent serial no. 16/325,923. No disclosures were reported by the other authors.

Authors' Contributions

D.C. Chung: Conceptualization, data curation, software, formal analysis, validation, investigation, visualization, methodology, writing–original draft, writing–review and editing. **N. Shakfa:** Data curation, software, formal analysis, methodology, writing–review and editing. **J. Vakharia:** Software, formal analysis, methodology. **K. Warner:** Data curation, writing–review and editing. **N. Jacquelot:** Data curation, writing–review and editing. **A. Sayad:** Software, formal analysis, writing–review and editing. **S. Han:** Data curation, writing–review and editing. **M. Ghaedi:** Data curation, writing–review and editing. **C.R. Garcia-Batres:** Data curation, writing–review and editing. **J. Sotty:** Data curation, writing–review and editing. **A. Azarmina:** Software, formal analysis. **F. Nowlan:** Software. **E.L.Y. Chen:** Methodology. **M. Zon:** Formal analysis. **A.R. Elford:** Resources, project administration. **B.X. Wang:** Resources, project administration, writing–review and editing. **L.T. Nguyen:** Resources, project administration, writing–review and editing. **M. Mrkonjic:** Resources. **B.A. Clarke:** Resources. **M.Q. Bernardini:** Resources. **B. Haibe-Kains:** Formal analysis. **S.E. Ferguson:** Resources. **S.Q. Crome:** Formal analysis, writing–review and editing. **H.W. Jackson:** Resources, project administration, writing–review and editing. **P.S. Ohashi:** Conceptualization, supervision, funding acquisition, writing–original draft, project administration, writing–review and editing.

Acknowledgments

We would like to thank the past and present members of the Ohashi Laboratory for technical help and scientific discussions, including Michael St. Paul, Meghan Kates, Ning An, Aras Toker, Khalid Dhuban, and Stephanie Wong. We would also like to thank Somi Afuni from the Jackson lab for her computational help. Furthermore, we thank the Princess Margaret Cancer Center Flow Facility and Princess Margaret Genomics Center for their technical support. Special acknowledgements are made to Drs. Arthur Mortha and Matthew Buechler for their suggestions and insights for this project. We would like to note that the Canadian Cancer Society grant was generously funded in memory of Jim JoTak, and the Wolfond Immunotherapy Fund at the Princess Margaret Cancer Foundation was generously donated by the Wolfond Family. We would also like to thank NIH for providing tetramers to MR1 and CD1d. This work was supported by the following grants: CIHR foundation award (CIHR FDN #143220), TRANSCAN Canadian Institutes of Health Research grant (CIHR – TRN #184713), Canadian Cancer Society (CCSRI #706152), Canadian Cancer Society grant (CHRYSALIDS TRANSCAN 3), and the Wolfond Immunotherapy Fund.

Note

Supplementary data for this article are available at Cancer Immunology Research Online (http://cancerimmunolres.aacrjournals.org/).

Received February 13, 2024; revised October 10, 2024; accepted February 11, 2025; published first February 14, 2025.

References

1. Vivier E, Artis D, Colonna M, Diefenbach A, Di Santo JP, Eberl G, et al. Innate lymphoid cells: 10 years on. Cell 2018;174:1054–66.
2. Bernink JH, Krabbendam L, Germar K, de Jong E, Gronke K, Kofoed-Nielsen M, et al. Interleukin-12 and -23 control plasticity of CD127+ group 1 and group 3 innate lymphoid cells in the intestinal lamina propria. Immunity 2015;43:146–60.
3. Vonarbourg C, Mortha A, Bui VL, Hernandez PP, Kiss EA, Hoyler T, et al. Regulated expression of nuclear receptor RORγt confers distinct functional fates to NK cell receptor-expressing RORγt+ innate lymphocytes. Immunity 2010;33:736–51.
4. Crinier A, Kerdiles Y, Vienne M, Cózar B, Vivier E, Berruyer C. Multidimensional molecular controls defining NK/ILC1 identity in cancers. Semin Immunol 2021;52:101424.
5. Sojka DK, Plougastel-Douglas B, Yang L, Pak-Wittel MA, Artyomov MN, Ivanova Y, et al. Tissue-resident natural killer (NK) cells are cell lineages distinct from thymic and conventional splenic NK cells. Elife 2014;3:e01659.
6. Lanier LL, Le AM, Civin CI, Loken MR, Phillips JH. The relationship of CD16 (Leu-11) and Leu-19 (NKH-1) antigen expression on human peripheral blood NK cells and cytotoxic T lymphocytes. J Immunol 1986;136:4480–6.
7. Wagner JA, Rosario M, Romee R, Berrien-Elliott MM, Schneider SE, Leong JW, et al. CD56bright NK cells exhibit potent antitumor responses following IL-15 priming. J Clin Invest 2017;127:4042–58.
8. Poznanski SM, Nham T, Chew MV, Lee AJ, Hammill JA, Fan IY, et al. Expanded CD56superbrightCD16+ NK cells from ovarian cancer patients are cytotoxic against autologous tumor in a patient-derived xenograft murine model. Cancer Immunol Res 2018;6:1174–85.
9. Dubois S, Conlon KC, Müller JR, Hsu-Albert J, Beltran N, Bryant BR, et al. IL15 infusion of cancer patients expands the subpopulation of cytotoxic CD56bright NK cells and increases NK-cell cytokine release capabilities. Cancer Immunol Res 2017;5:929–38.
10. Dowell AC, Oldham KA, Bhatt RI, Lee SP, Searle PF. Long-term proliferation of functional human NK cells, with conversion of CD56dim NK cells to a CD56bright phenotype, induced by carcinoma cells co-expressing 4-1BBL and IL-12. Cancer Immunol Immunother 2012;61:615–28.
11. Messaoudene M, Fregni G, Fourmentraux-Neves E, Chanal J, Maubec E, Mazouz-Dorval S, et al. Mature cytotoxic CD56bright/CD16+ natural killer cells can infiltrate lymph nodes adjacent to metastatic melanoma. Cancer Res 2014;74:81–92.
12. Netskar H, Pfefferle A, Goodridge JP, Sohlberg E, Dufva O, Teichmann SA, et al. Pan-cancer profiling of tumor-infiltrating natural killer cells through transcriptional reference mapping. Nat Immunol 2024;25:1445–59.
13. Jaeger N, Antonova AU, Kreisel D, Roan F, Lantelme E, Ziegler SF, et al. Diversity of group 1 innate lymphoid cells in human tissues. Nat Immunol 2024;25:1460–73.
14. Chung DC, Jacquelot N, Ghaedi M, Warner K, Ohashi PS. Innate lymphoid cells: role in immune regulation and cancer. Cancers (Basel) 2022;14:2071.
15. Fort MM, Leach MW, Rennick DM. A role for NK cells as regulators of CD4+ T cells in a transfer model of colitis. J Immunol 1998;161:3256–61.
16. Ehlers M, Papewalis C, Stenzel W, Jacobs B, Meyer KL, Deenen R, et al. Immunoregulatory natural killer cells suppress autoimmunity by down-regulating antigen-specific CD8+ T cells in mice. Endocrinology 2012;153:4367–79.
17. Laroni A, Armentani E, Kerlero de Rosbo N, Ivaldi F, Marcenaro E, Sivori S, et al. Dysregulation of regulatory CD56bright NK cells/T cells interactions in multiple sclerosis. J Autoimmun 2016;72:8–18.
18. Leavenworth JW, Wang X, Wenander CS, Spee P, Cantor H. Mobilization of natural killer cells inhibits development of collagen-induced arthritis. Proc Natl Acad Sci U S A 2011;108:14584–9.
19. Lee I-F, Qin H, Trudeau J, Dutz J, Tan R. Regulation of autoimmune diabetes by complete freund's adjuvant is mediated by NK cells. J Immunol 2004;172:937–42.
20. Smeltz RB, Wolf NA, Swanborg RH. Inhibition of autoimmune T cell responses in the DA rat by bone marrow-derived NK cells in vitro: implications for autoimmunity. J Immunol 1999;163:1390–7.
21. Lang PA, Crome SQ, Xu HC, Lang KS, Chapatte L, Deenick EK, et al. NK cells regulate CD8+ T cell mediated autoimmunity. Front Cell Infect Microbiol 2020;10:36.
22. Lu L, Ikizawa K, Hu D, Werneck MBF, Wucherpfennig KW, Cantor H. Regulation of activated CD4+ T cells by NK cells via the Qa-1-NKG2A inhibitory pathway. Immunity 2007;26:593–604.

23. Cao D, Hu L, Wang Y, Wang L, Zheng W, Ma W. Suppression of graft-versus-host disease after adoptive infusion of alloreactive NK cells induced by silencing Ly49C gene in mice. Transpl Immunol 2009;20:243–8.
24. Sivori S, Carlomagno S, Falco M, Romeo E, Moretta L, Moretta A. Natural killer cells expressing the KIR2DS1-activating receptor efficiently kill T-cell blasts and dendritic cells: implications in haploidentical HSCT. Blood 2011; 117:4284–92.
25. Lauener MP, AzadPour S, Abdossamadi S, Parthasarathy V, Ng B, Ostroumov E, et al. $CD56^{bright}CD16^{-}$ natural killer cells as an important regulatory mechanism in chronic graft-versus-host disease. Haematologica 2023;108:761–71.
26. Waggoner SN, Cornberg M, Selin LK, Welsh RM. Natural killer cells act as rheostats modulating antiviral T cells. Nature 2011;481:394–8.
27. Lang PA, Lang KS, Xu HC, Grusdat M, Parish IA, Recher M, et al. Natural killer cell activation enhances immune pathology and promotes chronic infection by limiting $CD8^{+}$ T-cell immunity. Proc Natl Acad Sci U S A 2012; 109:1210–5.
28. Zwirner NW, Domaica CI, Fuertes MB. Regulatory functions of NK cells during infections and cancer. J Leukoc Biol 2021;109:185–94.
29. Shi F-D, Van Kaer L. Reciprocal regulation between natural killer cells and autoreactive T cells. Nat Rev Immunol 2006;6:751–60.
30. Jegatheeswaran S, Mathews JA, Crome SQ. Searching for the elusive regulatory innate lymphoid cell. J Immunol 2021;207:1949–57.
31. Picard E, Godet Y, Laheurte C, Dosset M, Galaine J, Beziaud L, et al. Circulating $NKp46^{+}$ natural Killer cells have a potential regulatory property and predict distinct survival in Non-Small Cell Lung Cancer. Oncoimmunology 2019;8:e1527498.
32. Crome SQ, Nguyen LT, Lopez-Verges S, Yang SYC, Martin B, Yam JY, et al. A distinct innate lymphoid cell population regulates tumor-associated T cells. Nat Med 2017;23:368–75.
33. Liu Y, Song Y, Lin D, Lei L, Mei Y, Jin Z, et al. NCR^{-} group 3 innate lymphoid cells orchestrate IL-23/IL-17 axis to promote hepatocellular carcinoma development. EBioMedicine 2019;41:333–44.
34. Neo SY, Yang Y, Record J, Ma R, Chen X, Chen Z, et al. CD73 immune checkpoint defines regulatory NK cells within the tumor microenvironment. J Clin Inves 2020;130:1185–98.
35. Toker A, Nguyen LT, Stone SC, Yang SYC, Katz SR, Shaw PA, et al. Regulatory T cells in ovarian cancer are characterized by a highly activated phenotype distinct from that in melanoma. Clin Cancer Res 2018; 24:5685–96.
36. Yoshihara K, Tajima A, Yahata T, Kodama S, Fujiwara H, Suzuki M, et al. Gene expression profile for predicting survival in advanced-stage serous ovarian cancer across two independent datasets. PLoS One 2010;5:e9615.
37. Ferriss JS, Kim Y, Duska L, Birrer M, Levine DA, Moskaluk C, et al. Multigene expression predictors of single drug responses to adjuvant chemotherapy in ovarian carcinoma: predicting platinum resistance. PLoS One 2012;7: e30550.
38. Pils D, Hager G, Tong D, Aust S, Heinze G, Kohl M, et al. Validating the impact of a molecular subtype in ovarian cancer on outcomes: a study of the OVCAD Consortium. Cancer Sci 2012;103:1334–41.
39. The Cancer Genome Atlas Research Network, et al. Integrated genomic analyses of ovarian carcinoma. Nature 2011;474:609–15.
40. Tothill RW, Tinker AV, George J, Brown R, Fox SB, Lade S, et al. Novel molecular subtypes of serous and endometrioid ovarian cancer linked to clinical outcome. Clin Cancer Res 2008;14:5198–208.
41. Mateescu B, Batista L, Cardon M, Gruosso T, De Feraudy Y, Mariani O, et al. MiR-141 and miR-200a act on ovarian tumorigenesis by controlling oxidative stress response. Nat Med 2011;17:1627–35.
42. Dobin A, Davis CA, Schlesinger F, Drenkow J, Zaleski C, Jha S, et al. STAR: ultrafast universal RNA-seq aligner. Bioinformatics 2013;29:15–21.
43. Frankish A, Diekhans M, Ferreira A-M, Johnson R, Jungreis I, Loveland J, et al. GENCODE reference annotation for the human and mouse genomes. Nucleic Acids Res 2019;47:D766–73.
44. Li B, Dewey CN. RSEM: accurate transcript quantification from RNA-Seq data with or without a reference genome. BMC Bioinformatics 2011;12:323.
45. Huber W, Carey VJ, Gentleman R, Anders S, Carlson M, Carvalho BS, et al. Orchestrating high-throughput genomic analysis with Bioconductor. Nat Methods 2015;12:115–21.
46. Durinck S, Spellman PT, Birney E, Huber W. Mapping identifiers for the integration of genomic datasets with the R/Bioconductor package biomaRt. Nat Protoc 2009;4:1184–91.
47. Love MI, Huber W, Anders S. Moderated estimation of fold change and dispersion for RNA-seq data with DESeq2. Genome Biol 2014;15:550.
48. Benjamini Y, Hochberg Y. Controlling the false discovery rate: a practical and powerful approach to multiple testing. J R Stat Soc Ser B Methodol 1995;57: 289–300.
49. Subramanian A, Tamayo P, Mootha VK, Mukherjee S, Ebert BL, Gillette MA, et al. Gene set enrichment analysis: a knowledge-based approach for interpreting genome-wide expression profiles. Proc Natl Acad Sci U S A 2005;102: 15545–50.
50. Shannon P, Markiel A, Ozier O, Baliga NS, Wang JT, Ramage D, et al. Cytoscape: a software Environment for integrated models of biomolecular interaction networks. Genome Res 2003;13:2498–504.
51. Isserlin R, Merico D, Voisin V, Bader GD. Enrichment Map–a Cytoscape app to visualize and explore OMICs pathway enrichment results. F1000Res 2014;3:141.
52. Stuart T, Butler A, Hoffman P, Hafemeister C, Papalexi E, Mauck WM III, et al. Comprehensive integration of single-cell data. Cell 2019;177:1888–902.e21.
53. Haghverdi L, Lun ATL, Morgan MD, Marioni JC. Batch effects in single-cell RNA-sequencing data are corrected by matching mutual nearest neighbors. Nat Biotechnol 2018;36:421–7.
54. Kong GL, Nguyen TT, Rosales WK, Panikar AD, Cheney JHW, Lusardi TA, et al. CITEViz: interactively classify cell populations in CITE-Seq via a flow cytometry-like gating workflow using R-Shiny. BMC Bioinformatics 2024;25:142.
55. Aibar S, González-Blas CB, Moerman T, Huynh-Thu VA, Imrichova H, Hulselmans G, et al. SCENIC: single-cell regulatory network inference and clustering. Nat Methods 2017;14:1083–6.
56. Nguyen LT, Yen PH, Nie J, Liadis N, Ghazarian D, Al-Habeeb A, et al. Expansion and characterization of human melanoma tumor-infiltrating lymphocytes (TILs). PLoS One 2010;5:e13940.
57. Chevrier S, Crowell HL, Zanotelli VRT, Engler S, Robinson MD, Bodenmiller B. Compensation of signal spillover in suspension and imaging mass cytometry. Cell Syst 2018;6:612–20.e5.
58. Schapiro D, Jackson HW, Raghuraman S, Fischer JR, Zanotelli VRT, Schulz D, et al. HistoCAT: analysis of cell phenotypes and interactions in multiplex image cytometry data. Nat Methods 2017;14:873–6.
59. Greenwald NF, Miller G, Moen E, Kong A, Kagel A, Dougherty T, et al. Whole-cell segmentation of tissue images with human-level performance using large-scale data annotation and deep learning. Nat Biotechnol 2022; 40:555–65.
60. Eling N, Damond N, Hoch T, Bodenmiller B. cytomapper: an R/Bioconductor package for visualization of highly multiplexed imaging data. Bioinformatics 2020;36:5706–8.
61. Ronteix G, Aristov A, Bonnet V, Sart S, Sobel J, Esposito E, et al. Griottes: a generalist tool for network generation from segmented tissue images. BMC Biol 2022;20:178.
62. Shannon MJ, Mace EM. Natural killer cell integrins and their functions in tissue residency. Front Immunol 2021;12:647358.
63. Park SL, Gebhardt T, Mackay LK. Tissue-resident memory T cells in cancer immunosurveillance. Trends Immunol 2019;40:735–47.
64. Cerwenka A, Lanier LL. Natural killer cells, viruses and cancer. Nat Rev Immunol 2001;1:41–9.
65. Dogra P, Rancan C, Ma W, Toth M, Senda T, Carpenter DJ, et al. Tissue determinants of human NK cell development, function, and residence. Cell 2020;180:749–63.e13.
66. Cella M, Gamini R, Sécca C, Collins PL, Zhao S, Peng V, et al. Subsets of ILC3−ILC1-like cells generate a diversity spectrum of innate lymphoid cells in human mucosal tissues. Nat Immunol 2019;20:980–91.
67. Fuchs A, Vermi W, Lee JS, Lonardi S, Gilfillan S, Newberry RD, et al. Intraepithelial type 1 innate lymphoid cells are a unique subset of IL-12 and IL-15 responsive IFN-γ producing cells. Immunity 2013;38:769–81.
68. Huhn O, Ivarsson MA, Gardner L, Hollinshead M, Stinchcombe JC, Chen P, et al. Distinctive phenotypes and functions of innate lymphoid cells in human decidua during early pregnancy. Nat Commun 2020;11:381.
69. Webb JR, Milne K, Watson P, DeLeeuw RJ, Nelson BH. Tumor-infiltrating lymphocytes expressing the tissue resident memory marker CD103 are associated with increased survival in high-grade serous ovarian cancer. Clin Cancer Res 2014;20:434–44.
70. Yenyuwadee S, Luis J, Lopez JLS-T, Shah R, Rosato PC, Boussiotis VA. The evolving role of tissue-resident memory T cells in infections and cancer. Sci Adv 2022;8:eabo5871.

71. Zhu Y, Yao S, Iliopoulou BP, Han X, Augustine MM, Xu H, et al. B7-H5 costimulates human T cells via CD28H. Nat Commun 2013;4:2043.
72. Rajagopalan S, Long EO. KIR2DL4 (CD158d): an activation receptor for HLA-G. Front Immunol 2012;3:258.
73. Erokhina SA, Streltsova MA, Kanevskiy LM, Grechikhina MV, Sapozhnikov AM, Kovalenko EI. HLA-DR-expressing NK cells: effective killers suspected for antigen presentation. J Leukoc Biol 2021;109:327–37.
74. Roncarolo MG, Bigler M, Haanen JB, Yssel H, Bacchetta R, de Vries JE, et al. Natural killer cell clones can efficiently process and present protein antigens. J Immunol 1991;147:781–7.
75. Costa-García M, Ataya M, Moraru M, Vilches C, López-Botet M, Muntasell A. Human cytomegalovirus antigen presentation by HLA-DR$^+$ NKG2C$^+$ adaptive NK cells specifically activates polyfunctional effector memory CD4$^+$ T lymphocytes. Front Immunol 2019;10:687.
76. Burt BM, Plitas G, Nguyen HM, Stableford JA, Bamboat ZM, DeMatteo RP. Circulating HLA-DR$^+$ natural killer cells have potent lytic ability and weak antigen-presenting cell function. Hum Immunol 2008;69:469–74.
77. Voynova EN, Skinner J, Bolland S. Expansion of an etypical NK cell subset in mouse models of systemic lupus erythematosus. J Immunol 2015;194:1503–13.
78. Zhou J, Peng H, Li K, Qu K, Wang B, Wu Y, et al. Liver-resident NK cells control antiviral activity of hepatic T cells via the PD-1-PD-L1 axis. Immunity 2019;50:403–17.e4.
79. Zhang J, Chen Z, Smith GN, Croy BA. Natural killer cell-triggered vascular transformation: maternal care before birth? Cell Mol Immunol 2011;8:1–11.
80. Waggoner SN, Taniguchi RT, Mathew PA, Kumar V, Welsh RM. Absence of mouse 2B4 promotes NK cell-mediated killing of activated CD8$^+$ T cells, leading to prolonged viral persistence and altered pathogenesis. J Clin Invest 2010;120:1925–38.
81. Fernandez I, Zeiser R, Karsunky H, Kambham N, Beilhack A, Soderstrom K, et al. CD101 surface expression discriminates potency pmong murine FoxP3$^+$ regulatory T cells. J Immunol 2007;179:2808–14.
82. Shao L, Jacobs AR, Johnson VV, Mayer L. Activation of CD8$^+$ regulatory T cells by human placental trophoblasts. J Immunol 2005;174:7539–47.
83. Allez M, Brimnes J, Dotan I, Mayer L. Expansion of CD8$^+$ T cells with regulatory function after interaction with intestinal epithelial cells. Gastroenterology 2002;123:1516–26.
84. Bouloc A, Bagot M, Delaire S, Bensussan A, Boumsell L. Triggering CD101 molecule on human cutaneous dendritic cells inhibits T cell proliferation via IL-10 production. Eur J Immunol 2000;30:3132–9.
85. Schey R, Dornhoff H, Baier JLC, Purtak M, Opoka R, Koller AK, et al. CD101 inhibits the expansion of colitogenic T cells. Mucosal Immunol 2016;9:1205–17.
86. Marquardt N, Béziat V, Nyström S, Hengst J, Ivarsson MA, Kekäläinen E, et al. Cutting idge: identification and characterization of human tntrahepatic CD49a$^+$ NK cells. J Immunol 2015 194:2467–71.
87. Hudson WH, Gensheimer J, Hashimoto M, Wieland A, Valanparambil RM, Li P, et al. Proliferating sransitory T cells with an effector-like transcriptional signature emerge from PD-1$^+$ stem-like CD8$^+$ T cells during chronic infection. Immunity 2019;51:1043–58.e4.
88. Imianowski CJ, Whiteside SK, Lozano T, Evans AC, Benson JD, Courreges CJF, et al. BACH2 restricts NK cell maturation and function, limiting immunity to cancer metastasis. J Exp Med 2022;219:e20211476.
89. Zhong C, Zhu J. Transcriptional regulators dictate innate lymphoid cell fates. Protein Cell 2017;8:242–54.
90. Ebihara T, Song C, Ryu SH, Plougastel-Douglas B, Yang L, Levanon D, et al. Runx3 specifies lineage commitment of innate lymphoid cells. Nat Immunol 2015;16:1124–33.
91. Milner JJ, Toma C, Yu B, Zhang K, Omilusik K, Phan AT, et al. Runx3 programs CD8$^+$ T cell residency in non-lymphoid tissues and tumours. Nature 2017;552:253–7.
92. Wang D, Diao H, Getzler AJ, Rogal W, Frederick MA, Milner J, et al. The transcription factor Runx3 astablishes chromatin accessibility of cis-regulatory landscapes that drive memory cytotoxic T lymphocyte formation. Immunity 2018;48:659–74.e6.
93. Seehus CR, Kadavallore A, de la Torre B, Yeckes AR, Wang Y, Tang J, et al. Alternative activation generates IL-10 producing type 2 innate lymphoid cells. Nat Commun 2017;8:1900.
94. Benson MJ, Pino-Lagos K, Rosemblatt M, Noelle RJ. All-trans retinoic acid mediates enhanced T reg cell growth, differentiation, and gut homing in the face of high levels of co-stimulation. J Exp Med 2007;204:1765–74.
95. Spits H, Artis D, Colonna M, Diefenbach A, Di Santo JP, Eberl G, et al. Innate lymphoid cells–a proposal for uniform nomenclature. Nat Rev Immunol 2013;13:145–9.
96. Mouly E, Chemin K, Nguyen HV, Chopin M, Mesnard L, Leite-de-Moraes M, et al. The Ets-1 transcription factor controls the development and function of natural regulatory T cells. J Exp Med 2010;207:2113–25.
97. Sheng H, Marrero I, Maricic I, Fanchiang SS, Zhang S, Sant'Angelo DB, et al. Distinct PLZF$^+$CD8αα$^+$ unconventional T cells enriched in liver use a cytotoxic mechanism to limit autoimmunity. J Immunol 2019;203:2150–62.
98. Deaglio S, Dwyer KM, Gao W, Friedman D, Usheva A, Erat A, et al. Adenosine generation catalyzed by CD39 and CD73 expressed on regulatory T cells mediates immune suppression. J Exp Med 2007;204:1257–65.
99. Gu J, Ni X, Pan X, Lu H, Lu Y, Zhao J, et al. Human CD39^{hi} regulatory T cells present stronger stability and function under inflammatory conditions. Cell Mol Immunol 2017;14:521–8.
100. Yu L, Yang F, Zhang F, Guo D, Li L, Wang X, et al. CD69 enhances immunosuppressive function of regulatory T-cells and attenuates colitis by prompting IL-10 production. Cell Death Dis 2018;9:905.
101. Cortés JR, Sánchez-Díaz R, Bovolenta ER, Barreiro O, Lasarte S, Matesanz-Marín A, et al. Maintenance of immune tolerance by Foxp3$^+$ regulatory T cells requires CD69 expression. J Autoimmun 2014;55:51–62.
102. Lin C-R, Wei T-YW, Tsai H-Y, Wu Y-T, Wu P-Y, Chen S-T. Glycosylation-dependent interaction between CD69 and S100A8/S100A9 complex is required for regulatory T-cell differentiation. FASEB J 2015;29:5006–17.
103. Blanco-Domínguez R, de la Fuente H, Rodríguez C, Martín-Aguado L, Sánchez-Díaz R, Jiménez-Alejandre R, et al. CD69 expression on regulatory T cells protects from immune damage after myocardial infarction. J Clin Invest 2022;132:e152418.
104. Joller N, Lozano E, Burkett PR, Patel B, Xiao S, Zhu C, et al. Treg cells expressing the coinhibitory molecule TIGIT selectively inhibit proinflammatory Th1 and Th17 cell responses. Immunity 2014;40:569–81.
105. Kim EH, Gasper DJ, Lee SH, Plisch EH, Svaren J, Suresh M. Bach2 regulates homeostasis of Foxp3$^+$ regulatory T cells and protects against matal lung disease in mice. J Immunol 2014;192:985–95.
106. Garg G, Muschaweckh A, Moreno H, Vasanthakumar A, Floess S, Lepennetier G, et al. Blimp1 prevents methylation of Foxp3 and loss of regulatory T cell identity at sites of inflammation. Cell Rep 2019 26:1854–68.e5.
107. Ogawa C, Bankoti R, Nguyen T, Hassanzadeh-Kiabi N, Nadeau S, Porritt RA, et al. Blimp-1 functions as a molecular switch to prevent inflammatory activity in Foxp3$^+$RORγt$^+$ regulatory T cells. Cell Rep 2018;25:19–28.e5.
108. Lee S, Park K, Kim J, Min H, Seong RH. Foxp3 expression in induced regulatory T cells is stabilized by C/EBP in inflammatory environments. EMBO Rep 2018;19:e45995.
109. Alvisi G, Brummelman J, Puccio S, Mazza EMC, Tomada EP, Losurdo A, et al. IRF4 instructs effector Treg differentiation and immune suppression in human cancer. J Clin Invest 2020;130:3137–50.
110. Cretney E, Xin A, Shi W, Minnich M, Masson F, Miasari M, et al. The transcription factors Blimp-1 and IRF4 jointly control the differentiation and function of effector regulatory T cells. Nat Immunol 2011;12:304–11.
111. Ghosh A, Holland AM, Dogan Y, Yim NL, Rao UK, Young LF, et al. PLZF confers effector functions to donor T cells that preserve graft-versus-tumor effects while attenuating GVHD. Cancer Res 2013;73:4687–96.
112. Cella M, Otero K, Colonna M. Expansion of human NK-22 cells with IL-7, IL-2, and IL-1beta reveals intrinsic functional plasticity. Proc Natl Acad Sci U S A 2010;107:10961–6.
113. Yomogida K, Bigley TM, Trsan T, Gilfillan S, Cella M, Yokoyama WM, et al. Hobit confers tissue-dependent programs to type 1 innate lymphoid cells. Proc Natl Acad Sci U S A 2021;118:e2117965118.
114. Friedrich C, Taggenbrock RLRE, Doucet-Ladevèze R, Golda G, Moenius R, Arampatzi P, et al. Effector differentiation downstream of lineage commitment in ILC1s is driven by Hobit across tissues. Nat Immunol Nat Res 2021;22:1256–67.
115. Duhen T, Duhen R, Montler R, Moses J, Moudgil T, De Miranda NF, et al. Co-expression of CD39 and CD103 identifies tumor-reactive CD8 T cells in human solid tumors. Nat Commun 2018;9:2724.
116. Simoni Y, Becht E, Fehlings M, Loh CY, Koo S-L, Teng KWW, et al. Bystander CD8$^+$ T cells are abundant and phenotypically distinct in human tumour infiltrates. Nature 2018 557:575–9.
117. Schuster IS, Wikstrom ME, Brizard G, Coudert JD, Estcourt MJ, Manzur M, et al. TRAIL$^+$ NK cells control CD4$^+$ T cell responses during chronic viral infection to limit autoimmunity. Immunity 2014;41:646–56.

118. Schuster IS, Sng XYX, Lau CM, Powell DR, Weizman O-E, Fleming P, et al. Infection induces tissue-resident memory NK cells that safeguard tissue health. Immunity 2023;56:531–46.e6.
119. Cortez VS, Ulland TK, Cervantes-Barragan L, Bando JK, Robinette ML, Wang Q, et al. SMAD4 impedes the conversion of NK cells into ILC1-like cells by curtailing non-canonical TGF-β signaling. Nat Immunol 2017;18:995–1003.
120. Gao Y, Souza-Fonseca-Guimaraes F, Bald T, Ng SS, Young A, Ngiow SF, et al Tumor immunoevasion by the conversion of effector NK cells into type 1 innate lymphoid cells. Nat Immunol 2017;18:1004–15.
121. Chung DC, Garcia-Batres CR, Millar DG, Wong SWY, Elford AR, Mathews JA, et al. Generation of an inhibitory NK cell subset by TGF-β1/IL-15 polarization. J Immunol 2024;212:1904–12.
122. Chen M-L, Pittet MJ, Gorelik L, Flavell RA, Weissleder R, von Boehmer H, et al. Regulatory T cells suppress tumor-specific CD8 T cell cytotoxicity through TGF-signals in vivo. Proc Natl Acad Sci U S A 2005;102:419–24.
123. Mempel TR, Pittet MJ, Khazaie K, Weninger W, Weissleder R, von Boehmer H, et al. Regulatory T cells reversibly suppress cytotoxic T cell function independent of effector differentiation. Immunity 2006;25:129–41.
124. Haruna M, Ueyama A, Yamamoto Y, Hirata M, Goto K, Yoshida H, et al. The impact of $CCR8^+$ regulatory T cells on cytotoxic T cell function in human lung cancer. Sci Rep 2022;12:5377.
125. Xu HC, Grusdat M, Pandyra AA, Polz R, Huang J, Sharma P, et al. Type I interferon protects antiviral $CD8^+$ T cells from NK cell cytotoxicity. Immunity 2014;40:949–60.
126. Crouse J, Bedenikovic G, Wiesel M, Ibberson M, Xenarios I, VonLaer D, et al. Type I interferons protect T cells against NK cell attack mediated by the activating receptor NCR1. Cell Press 2014;40:961–73.
127. Xu HC, Huang J, Pandyra AA, Lang E, Zhuang Y, Thöns C, et al. Lymphocytes negatively regulate NK cell activity via Qa-1b following viral infection. Cell Rep 2017 21:2528–40.
128. Moreno-Nieves UY, Tay JK, Saumyaa S, Horowitz NB, Shin JH, Mohammad IA, et al. Landscape of innate lymphoid cells in human head and neck cancer reveals divergent NK cell states in the tumor microenvironment. Proc Natl Acad Sci U S A 2021 118:e2101169118.
129. Gao Q, Qiu S-J, Fan J, Zhou J, Wang X-Y, Xiao Y-S, et al. Intratumoral balance of regulatory and cytotoxic T cells is associated with prognosis of hepatocellular carcinoma after resection. J Clin Oncol 2007;25:2586–93.
130. Prizment AE, Vierkant RA, Smyrk TC, Tillmans LS, Nelson HH, Lynch CF, et al. Cytotoxic t cells and granzyme b associated with improved colorectal cancer survival in a prospective cohort of older women. Cancer Epidemiol Biomarkers Prev 2017;26:622–31.
131. Mizoguchi K, Kawaji H, Kai M, Morisaki T, Hayashi S, Takao Y, et al. Granzyme B expression in the tumor microenvironment as a prognostic eiomarker for patients with triple-negative breast cancer. Cancers (Basel) 2023;15:4456.
132. Zhu Y, Ferri-Borgogno S, Sheng J, Yeung T-L, Burks JK, Cappello P, et al. SIO: a spatioimageomics pipeline to identify prognostic biomarkers associated with the ovarian tumor microenvironment. Cancers (Basel) 2021;13:1777.
133. Tumeh PC, Harview CL, Yearley JH, Shintaku IP, Taylor EJM, Robert L, et al. PD-1 blockade induces responses by inhibiting adaptive immune resistance. Nature 2014;515:568–71.
134. Amaria RN, Reddy SM, Tawbi HA, Davies MA, Ross MI, Glitza IC, et al. Neoadjuvant immune checkpoint blockade in high-risk resectable melanoma. Nat Med 2018;24:1649–54.
135. Chen P-L, Roh W, Reuben A, Cooper ZA, Spencer CN, Prieto PA, et al. Analysis of immune signatures in longitudinal tumor samples yields insight into biomarkers of response and mechanisms of resistance to immune checkpoint blockade. Cancer Discov 2016;6:827–37.
136. Zhang Y, Chen H, Mo H, Hu X, Gao R, Zhao Y, et al. Single-cell analyses reveal key immune cell subsets associated with response to PD-L1 blockade in triple-negative breast cancer. Cancer Cell 2021;39:1578–93.e8.
137. Bassez A, Vos H, Van Dyck L, Floris G, Arijs I, Desmedt C, et al. A single-cell map of intratumoral changes during anti-PD1 treatment of patients with breast cancer. Nat Med 2021;27:820–32.
138. Wang XQ, Danenberg E, Huang C-S, Egle D, Callari M, Bermejo B, et al. Spatial predictors of immunotherapy response in triple-negative breast cancer. Nature 2023;621:868–76.
139. Zheng L, Qin S, Si W, Wang A, Xing B, Gao R, et al. Pan-cancer single-cell landscape of tumor-infiltrating T cells. Science 2021;374:abe6474.
140. Tietscher S, Wagner J, Anzeneder T, Langwieder C, Rees M, Sobottka B, et al. A comprehensive single-cell map of T cell exhaustion-associated immune environments in human breast cancer. Nat Commun 2023;14:98.
141. Gruosso T, Gigoux M, Manem VSK, Bertos N, Zuo D, Perlitch I, et al. Spatially distinct tumor immune microenvironments stratify triple-negative breast cancers. J Clin Invest 2019;129:1785–800.
142. Maiorano BA, Maiorano MFP, Lorusso D, Maiello E. Ovarian cancer in the era of immune checkpoint Inhibitors: state of the art and future perspectives. Cancers (Basel) 2021;13:4438.